Ore Geology Reviews 126 (2020) 103720

Contents lists available at ScienceDirect

Ore Geology Reviews

journal homepage: www.elsevier.com/locate/oregeorev

The evolution of metasomatic uranium ore systems in the Kitts-Post Hill belt of the Central Mineral Belt, Labrador, Canada

Charlene L. Duffett[a,*], Eric G. Potter[b], Duane C. Petts[b], Pedro Acosta-Gongóra[b], Brian L. Cousens[a], Greg W. Sparkes[c]

[a] Ottawa-Carleton Geoscience Centre, Carleton University, 1125 Colonel By Drive, Ottawa, ON K1S5B6, Canada
[b] Geological Survey of Canada, 601 Booth St., Ottawa, On K1A 0E8, Canada
[c] Government of Newfoundland and Labrador, Department of Natural Resources, Geological Survey, St. John's, NL, A1B 4J6, Canada

ARTICLE INFO

Keywords:
IOAA
Central Mineral Belt
Uranium
Magnetite
Metasomatic
Kitts

ABSTRACT

Uranium mineralization in the Kitts-Post Hill belt of the Central Mineral Belt (CMB) of Labrador, Canada is concentrated in the upper portion of the Paleoproterozoic Post Hill Group, along a structurally complex shear zone that developed during ca. 1860–1800 Ma orogenic events. Recent research in the CMB highlights regional- to deposit-scale features such as Na-, Ca-Fe-, K- and K-Fe- alteration and hydrothermal breccia zones characteristic of iron oxide and alkali-calcic alteration systems that host iron oxide-copper–gold (IOCG) and affiliated deposits. Potential genetic links between the CMB uranium district and metasomatic systems hosting IOCG deposits was explored through petrography and trace element chemistry of uraninite. The least-altered uraninite grains from mineral occurrences in the Kitts-Post Hill belt contain elevated Th, Zr, Y and rare earth element (REE) contents, implying primary uranium mineralization from high temperature, alkaline fluids capable of transporting high field-strength elements – similar to deposits in iron oxide and alkali-calcic alteration systems. Quantitative LA-ICP-MS mapping of uraninite at the Kitts deposit demonstrates remobilization of U, Pb and light-REE along grain boundaries and fractures, coupled with zones of elevated Zr, and lower Th and REE contents that record element leaching during alteration and/or recrystallization. In chondrite-normalized REE plots of uraninite, contrasting REE patterns define three populations of uraninite grains that formed under different temperature and physico-chemical conditions. Leaching of light-REE from uraninite grains support recent studies that indicate light-REE signatures of uraninite can be disturbed under certain conditions, whereas the primary signatures of heavy-REE remain preserved. The inferred contrasting fluid sources revealed by the major and trace element composition of uraninite suggest that metasomatism and mineralization involved a complex and evolving fluid history, complicated by post-ore magmatism and metamorphism.

1. Introduction

The Central Mineral Belt (CMB) is a well-known uranium district located within central Labrador, Canada (Fig. 1a) that hosts multiple uranium-bearing polymetallic showings, prospects and undeveloped deposits in Neoarchean to Mesoproterozoic rocks (e.g., Gower et al., 1982; Ryan, 1984; Kerr et al., 1996; Sparkes et al., 2016; Sparkes, 2017). Exploration in the area commenced in the 1960s and proceeded to feasibility studies in the early 1980s, with emphasis on the Michelin and Kitts deposits. After two decades of limited activity, the region experienced a surge in exploration activity from 2003 to 2009, and resources at the Michelin deposit were significantly expanded (e.g., Sparkes and Kerr, 2008; Sparkes, 2017). In the CMB, several types of uranium mineralization are now recognized, including metasomatic or albitite-hosted (e.g., Michelin deposit), iron oxide-rich veins and breccias (e.g., Moran Lake Upper C Zone) and sedimentary-hosted (e.g., Moran Lake Lower C Zone and Anna Lake deposits) (Sparkes and Kerr, 2008; Sparkes, 2017; Sparkes et al., 2016, 2017). The uranium mineral occurrences and host rocks of the CMB are characterized by regional- to deposit-scale Na-, Ca-Fe-, K- and K-Fe-rich alteration (Acosta-Góngora et al., 2018), as well as iron oxide-rich hydrothermal breccia (Sparkes and Kerr, 2008); all characteristic of iron oxide and alkali-calcic (IOAA) systems that host iron oxide-copper–gold (IOCG) deposits (Corriveau et al., 2010, 2016). Sparkes (2017) and Sparkes et al. (2017) proposed two uranium mineralization events in the eastern CMB at 2030–1880 Ma and 1860–1800 Ma, that overlap in part with ages of

* Corresponding author.
E-mail address: charleneduffett@cmail.carleton.ca (C.L. Duffett).

https://doi.org/10.1016/j.oregeorev.2020.103720
Received 3 April 2020; Received in revised form 7 August 2020; Accepted 10 August 2020
Available online 14 August 2020
0169-1368/ Crown Copyright © 2020 Published by Elsevier B.V. All rights reserved.

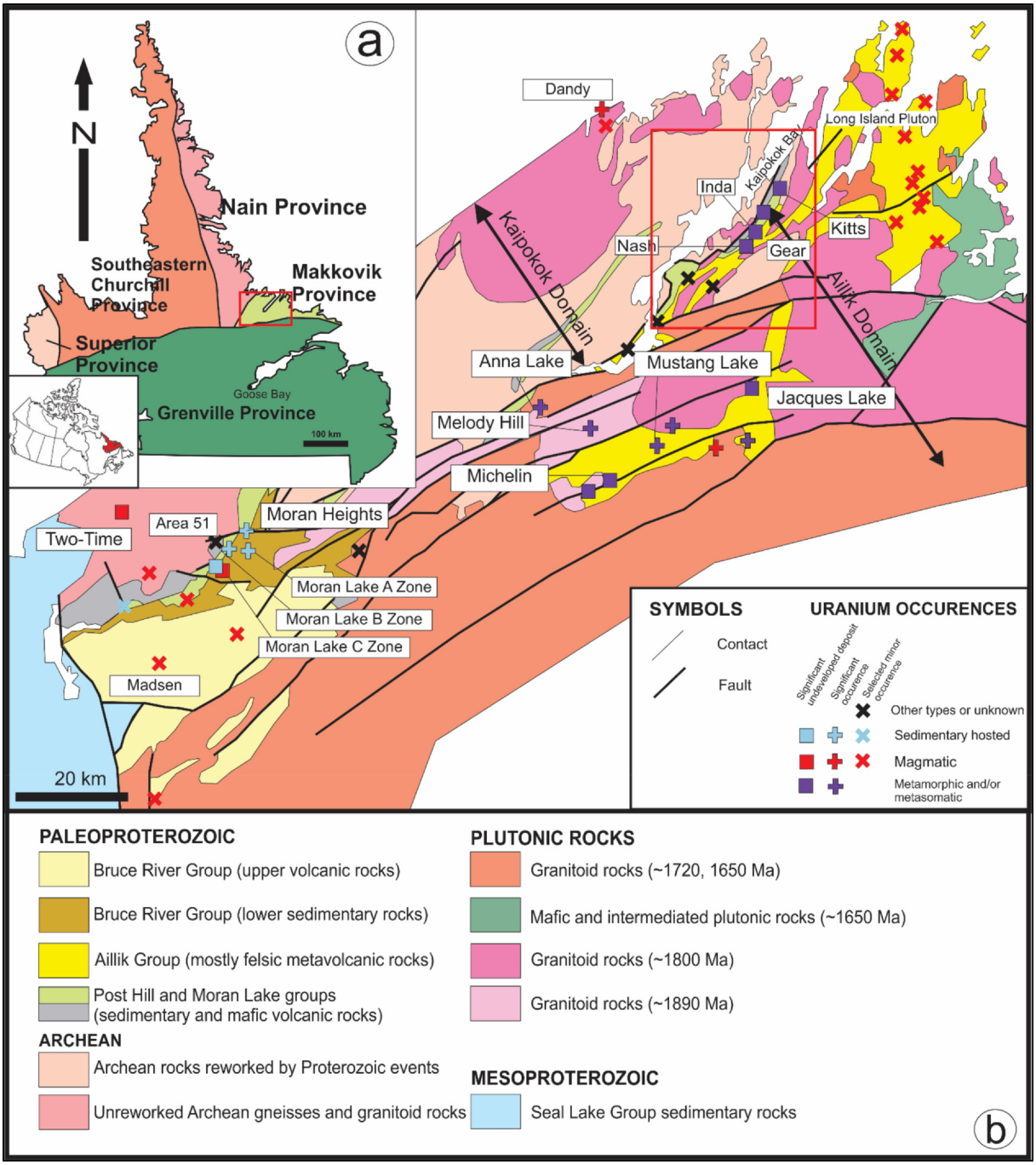


Fig. 1. (a) Location and geology of Labrador; (b) Geology of the Central Mineral Belt, with locations of deposits and showings of uranium mineralization, modified from Sparkes and Kerr (2008).

mineralization proposed for the uranium occurrences in the western CMB (1860–1660 Ma; Sparkes, 2017) and regional orogenic events. The regional-scale alteration, combined with the timing of uranium mineralization, provide possible evidence to link the primary mineralization to regional-scale IOAA systems, followed by reworking during younger intrusive, orogenic and metamorphic events.

Since discovery of the Olympic Dam deposit in Australia in the 1970s and subsequent definition of the IOCG deposit type in the 1990s (Hitzman et al., 1992), these deposits have been attractive targets for exploration. In addition to the potential for huge tonnages (e.g., Olympic Dam has resources of 10,100 Mt at 0.78% Cu, 0.25 kg/t U_3O_8, 0.33 g/t Au and 1 g/t Ag; BHP, 2018), IOCG deposits also represent a significant source of uranium, with Olympic Dam containing the world's largest recoverable source of uranium (OECD, 2018). To encapsulate the regional- to local-scale alteration and range of deposit types characteristic of these systems, Porter (2010a,b), Corriveau et al. (2010) and Corriveau et al. (2016, in press) propose adoption of the term "iron oxide and alkali-calcic alteration" (IOAA) ore system. These systems can host IOCG deposits, *senso stricto*, but also several affiliated deposit types including albitite-hosted uranium. Although a genetic link between albitite-hosted uranium and IOCG deposits was recently proposed in the Great Bear magmatic zone (Montreuil et al., 2015; Potter et al., 2019), this linkage remains controversial, and albitite-hosted uranium was previously associated to carbonatite and/or alkaline magma emplacement (Wilde, 2013).

In this contribution, detailed petrographic information is combined

with quantitative major and trace element maps of uraninite to examine the source(s) of uranium and conditions of ore formation in the polymetallic (U ± Fe, Cu, Au, REE) metasomatic ore deposits of the Kitts-Post Hill trend located in the northeast CMB (Fig. 1). This study focuses on the four main deposits in this area, namely Kitts, Inda, Gear and Nash deposits (Fig. 1). The geochemical signatures of uraninite from the studied CMB deposits are compared to those of other uranium deposits and IOAA systems elsewhere to assess potential genetic links between the CMB uranium district and IOAA systems. This hypothesis will be tested in collaboration with other studies (Acosta-Góngora et al., submitted.) in an attempt to unite the Kitts-Post Hill belt with other deposits of the CMB.

1.1. Iron oxide and alkali-calcic systems

The IOAA ore system model of Porter (2010a,b), updated by Corriveau et al. (2010, 2016, in press), explains the development of IOCG deposits from their early, high-temperature and deep-seated Na alteration (formation of albitite) to later, shallower and lower-temperature epithermal settings (e.g., silicification and argillic alteration). This alteration path aligns with the systematic emplacement of a series of metasomatic alteration types observed, allowing for seemingly disparate showings over a large area to be explained by a single ore system model.

Development of IOAA systems requires large volumes of hot, saline fluids that interact with host rocks over several square kilometers, generally through large-scale crustal fault systems, and are driven by calc-alkaline to shoshonitic, high-temperature magmatism, repeated dyke emplacement and active tectonic regimes that promote fluid circulation and heat transfer (Corriveau et al., 2016; Montreuil et al., 2015). The high-temperature Na- to Ca-Fe-alteration zones are early, pervasive and intense, and demarcate areas of interest or may form the host to magnetite-apatite (iron oxide-apatite or IOA) deposits. Evolution of high-temperature K-Fe-alteration (magnetite-K-feldspar/biotite), skarn assemblages (clinopyroxene/garnet) and then lower temperature K-Fe ($+H_2O$-CO_2) alteration assemblages (sericite/K-feldspar-hematite-chlorite-carbonate) can produce polymetallic IOCG deposits, some of which may contain elevated concentrations of uranium (Corriveau et al., 2010). Although original textures may be preserved or mimicked ('pseudomorphing'); texture-destructive recrystallization of protoliths is common within IOAA systems, resulting in alteration zones that are difficult to identify while mapping. However, using a "facies" approach reveals the systematic evolution of alteration assemblages from regional- to deposit-scales (Corriveau et al., 2010, 2016). Iron oxide-apatite deposits develop early in the IOAA system, at extremely high fluid temperatures (400–800 °C) and at deeper levels in the crust than magnetite-group (450–350 °C) or hematite-group (350–250 °C) IOCG deposits (Corriveau et al., 2016 and references therein).

Iron oxide-copper–gold and IOA deposits can both host large tonnages of metals, produced by large volumes of fluids that metasomatically alter the host rocks. These systems can host a variety of economically significant deposits (IOCG, IOA, albitite-hosted uranium, certain skarns and certain intrusion-related deposits) rich in base, precious and critical metals and/or actinides (Corriveau, 2007; Corriveau et al., 2010; Montreuil et al., 2015). These seemingly distinct deposit types form in a systematic metasomatic-hydrothermal alteration system from depth-to-surface across very high-temperature geothermal gradients within the upper crust, linked to magma chambers that evolve as metasomatism proceeds and geodynamic conditions change (Montreuil et al., 2016).

Albitite-hosted uranium deposits (also known as Na-metasomatic uranium), are characterized by extensive, porous albitite corridors along regional-scale shear zones that act as conduits for fluid flow (Cuney, 2009; Cuney et al., 2012). In these deposits, uranium ore minerals (uraninite-coffinite) and associated gangue minerals (hematite, carbonates, biotite or phlogopite, quartz and Fe-Cu-Pb-sulfides) are syngenetic with respect to Ca-Mg, K-and K-Fe alteration types, yet postdate early Na-metasomatism (e.g., Porto de Silveira et al., 1991; Polito et al., 2009; Cuney et al., 2012; Kontonikas-Charos et al., 2014; Montreuil et al., 2015). As illustrated by the Southern Breccia albitite-hosted uranium occurrence and NICO magnetite-group IOCG deposit in the Great Bear magmatic zone in Canada, albitite-hosted uranium and IOCG deposits can occur together within a single IOAA system (Montreuil et al., 2015; Potter et al., 2019). Although albitite corridors in IOAA systems are frequently barren in terms of metals, fluids responsible for Na alteration created the Southern Breccia albitite zone before it was thrusted upwards into cooler or more distal alteration facies of the system, which allowed for metal precipitation during later K-Fe alteration (Montreuil et al., 2015; Corriveau et al., 2016; Potter et al., 2019).

Historically, models for uranium enrichment in IOCG systems have invoked the incursion of oxidized fluids to transport mobile U^{6+} (e.g., Hitzman and Valenta, 2005; Skirrow, 2010). However, recent experimental work has noted the presence of a stable UCl_4 species under acidic and reduced conditions (Timofeev et al., 2018). Petrographic evidence and trace element data from uraninite led Potter et al. (in press) to propose that primary uranium precipitation in IOAA systems can occur during the reduced, high temperature K-Fe (magnetite) facies, as fluid temperatures decrease and the pH of the fluids change through fluid-rock interactions. In a recent geochemical study of both magnetite- and hematite-group IOCG deposits and prospects from the Gawler province in Australia, Fabris (in press) also noted that uranium enrichment in magnetite-dominated occurrences is commonly similar to or greater in magnitude than uranium enrichment in hematite-dominated occurrences, supporting primary uranium mineralization early in the development of these ore systems (i.e., during magnetite alteration). Subsequent dissolution-reprecipitation and remobilization of primary uraninite can occur during the transition to hematite-bearing K-Fe alteration, expanding the uranium potential in IOCG systems from magnetite-to hematite-bearing deposits (Potter et al., in press).

2. Regional geology

The CMB is located mostly within the Makkovik Province in Labrador, but also stretches into the adjoining Nain and Grenville geological provinces (Fig. 1). The largely Paleoproterozoic Makkovik Province is separated from the Archean Nain Province to the northwest by the Kanairiktok shear zone, and is bounded in the south by the Grenville Front, marking the northern structural limit of the Mesoproterozoic Grenville Province (Fig. 1a). This area of Labrador has been the focus of many geological studies focused on both the tectonic evolution (e.g., Schärer et al., 1988; Gower et al., 1982, 1992; Kerr et al., 1996; Ketchum et al., 2001, 2002; Hinchey, 2007) and economic potential (e.g., Gandhi, 1978; Wilton and Wardle, 1987; Wilton and Longerich, 1993; Sparkes, 2017).

This paper focuses on the Kaipokok and the Aillik domains of the Makkovik Province as defined by Gower and Ryan (1987), which are hosts to widespread uranium mineralization (Fig. 1b). The Makkovik Province is defined by the Makkovikian orogeny (1.85–1.75 Ga), and is an extension of the Ketilidian Mobile Belt in southern Greenland (Gower and Ryan, 1986; Kerr et al., 1996). The Aillik domain is separated from the Kaipokok domain by the Kaipokok Bay Structural Zone, a system of high-grade strain zones (Ketchum et al., 1997) that were active until 1805–1780 Ma, as determined by horneblende Ar-Ar geochronology (Culshaw et al., 2002). Archean basement rocks underlie the Kaipokok and Aillik domains, with ages defined for a tonalite gneiss at 2878^{+27}_{-16} Ma (Ketchum et al., 2001) and a migmatitic granodiorite gneiss at 2813^{+16}_{-13} Ma (Ketchum et al., 2002). The Kaipokok domain includes the ca. 2180 Ma Post Hill Group (Ketchum et al., 2002), a Paleoproterozoic supracrustal sequence metamorphosed to amphibolite facies. The Post Hill Group is dominated by metamorphosed siliciclastic

and mafic volcanic rocks, which are considered to be time-equivalent to the unmetamorphosed Moran Lake Group in the southwest of the CMB. Collectively, these sedimentary and metasedimentary rocks are interpreted as a passive margin-foredeep succession deposited on the North Atlantic Craton, represented by the adjacent Nain Province (Ketchum et al., 2002; Hinchey, 2007).

Rocks of the Kaipokok domain were reworked during the Makkovkian orogeny, when major zones of tectonic thrusting and thinning resulted in interleaving of the Archean basement and overlying Post Hill Group (Marten, 1977), development of a regional north-northeast tectonic fabric and shear zones, and greenschist to amphibolite facies metamorphism (Gower and Ryan, 1986; Ketchum et al., 1997). Uranium mineralization in the Kaipokok domain occurs largely in metasedimentary rocks of the Post Hill Group (Gandhi, 1978).

The Aillik domain is dominated by the 1860–1800 Ma Aillik Group (Schärer et al., 1988), which is composed of metavolcanic and metasedimentary rocks that are in tectonic contact with the older Post Hill Group (Marten, 1977; Gower et al., 1982; Kerr et al., 1996; Ketchum et al., 2002; Fig. 1b). Schärer et al. (1988) proposed that the Aillik Group formed during two distinct volcanic pulses, roughly coeval with the Makkovikian orogeny. Abundant calc-alkaline plutonic activity in the area, and extensional-setting mafic dykes which cut all units, indicate that the Aillik Group was deposited in a rifted-arc setting (Culshaw et al., 2000). The felsic metavolcanic rocks of the Aillik Group host numerous uranium occurrences, including the large Michelin deposit (Gandhi, 1978).

Late east–west trending faults occur throughout the Makkovik Province and are interpreted to have formed during the Labradorian or Grenvillian orogeny. The Labradorian orogeny was first described by Nunn et al. (1985) as a ca. 1650 Ma deformational-metamorphic event in the Grenville Province of south-west Labrador, distinct from the Trans-Hudson (2000–1800 Ma; Wardle et al., 1990) and later Grenville orogenies (1200–1000 Ma; Gower et al., 1992). Plutonic activity in the CMB was subdivided into three stages based on timing of emplacement: (1) syntectonic Makkovikian rocks emplaced between 1840 and 1800 Ma; (2) post-tectonic Makkovikian rocks emplaced between 1800 and 1720 Ma; and (3) Labradorian plutonic rocks emplaced between 1670 and 1630 Ma (Gower et al., 1992; Kerr et al., 1996). The Grenville Front marks the southern limit of the Makkovik Province and northern limit of ca. 1.0 Ga Grenvillian deformation, and notably no Grenvillian plutonism is found in the Makkovik Province (Gower and Ryan, 1986). The Grenville Front and related structures in Labrador are mostly high-angle reverse faults, whereas moderate- to low-angle thrusts occur more towards the interior of the Grenville Province (Gower and Ryan, 1986).

3. Local geology

The area of this study is comprised of two main geological units, namely the Post Hill and Aillik groups. In older literature, the Post Hill Group was termed the Lower Aillik Group, and the rocks now assigned to the Aillik Group were termed the Upper Aillik Group. The stratigraphic terminology was revised following recognition of the large age difference between the two sequences (Ketchum et al., 1997).

The Post Hill Group is subdivided into four lithologic units: (1) the Post Hill amphibolite, consisting of metavolcanic rocks; (2) the Metasedimentary formation; (3) the Kitts Pillow Lava formation, consisting of well-preserved volcanic rocks; and (4) the Drunken Harbour supracrustal belt (Marten, 1977; Ketchum et al., 2002). With the exception of the Drunken Harbour belt, these are shown in Figure 2. Basal quartzite units from the Post Hill Group were deposited prior to 2235 Ma, based on Archean dates acquired for detrital zircons from these units that define a maximum age of 2235 ± 2 Ma and a mafic dyke swarm dated at ca. 2235 Ma (Cadman et al., 1993) that does not intrude these units (Ketchum et al., 2002). Overlying the quartzite units are 2178 ± 4 Ma metavolcanic rocks of the Post Hill amphibolite, but the Metasedimentary formation (originally of turbidite affinity) gave a significantly younger age of ca. 2013 Ma (Ketchum et al., 2002).

The ca. 1860 Ma Aillik Group is in tectonic contact with the older Post Hill Group, and is subdivided into a lower unit consisting of various sedimentary units, dacite, rhyolite and mafic volcanic rocks, and an upper unit of felsic tuff, flow-banded rhyolite, sedimentary rocks and quartz feldspar porphyry (Gower and Ryan, 1987; Ketchum et al., 2002). Both units have greenschist to lower amphibolite facies metamorphic assemblages, are widely recrystallized and locally silicified, but also locally preserve some primary textures (Kerr et al., 1996; Ketchum et al., 2002).

A structurally complex shear zone separates the Post Hill Group in the northeast from the Aillik Group in the southwest, and hosts most of the Post Hill Group uranium mineralization, including the Kitts, Gear, Inda and Nash deposits (Fig. 2) (Gandhi, 1978). Uranium mineralization at Kitts, Gear, Inda and Nash is concentrated in the upper portion of the Post Hill Group, close to the contact with the Aillik Group, although sections of this contact can be difficult to distinguish (Sparkes, 2017). Zircon U-Pb (TIMS) geochronology from the Kitts metagabbro (interpreted to predate mineralization) yielded an age of 2018 $^{+15}_{-8}$ Ma. The Aillik Group is mostly unmineralized, although Evans (1980) noted widespread alkali metasomatism, similar to that of the Michelin deposit. Tracing of units along strike between the Kitts-Post Hill belt deposits is difficult due to the intense deformation in this area.

3.1. Classification of uranium mineralization in the region

Following the International Atomic Energy Agency (IAEA) classification (Bruneton et al., 2014), intrusive related or magmatic uranium deposits generally occur in the Archean basement rocks (e.g., Kanairiktok prospect) or in pegmatitic intrusions (e.g., Dandy prospect). Felsic volcanic rocks (e.g., Madsen and Melody Hill prospects) and mafic volcanic-hosted (e.g., Moran Lake Upper C Zone) host iron oxide-rich breccias classified as polymetallic hematite breccia complexes as per Bruneton et al. (2014). Sandstone-type uranium mineralization occurs mainly in the Moran Lake area (e.g., Moran Heights prospect and Moran Lower C Zone deposit) as well as black shale-type (e.g., Armstrong deposit) mineralization.

Metamorphite or metasomatic uranium (classification is still debated) is most prominent in the central portion of the CMB and includes some of the largest resources (e.g., Michelin and Jacques Lake deposits), as well as the deposits within the Kitts-Post Hill belt that are the subject of this paper. Although Gandhi (1978) proposed a syngenetic sedimentary classification for the Kitts deposit, both Evans (1980) and Sparkes (2017) suggest a structural control for these occurrences and propose that mineralizing fluids originated in part from metamorphic events.

3.2. Uranium deposits of the Kitts-Post Hill belt

The uranium mineralization from the Kitts-Post Hill belt is hosted by the Post Hill Group, but locally extends into the adjacent Aillik Group. Mineralization is primarily developed within argillite of the Metasedimentary formation, which is locally interbedded with the Kitts Pillow Lava formation. The mineralization is interpreted to be structurally constrained to foliation planes and shear zones (Sparkes, 2017).

Golder (1977) initially reported underground resource estimates for the Kitts deposit of 203,880 lbs of U_3O_8 at a grade of 0.73% (Note: this estimate predates NI-43-101 reporting standards). Paladin Energy Ltd. (2019) reported indicated underground resource estimates for Gear, Inda and Nash deposits of 532 000, 324 000 and 214 000 lbs of U_3O_8 at grades of 0.080%, 0.070% and 0.060% U_3O_8 that are compliant with the 2004 Australasian code for reporting of exploration results, mineral resources and ore reserves (JORC code).

The geology of the Kitts deposit (Fig. 3a) is dominated by the Kitts Pillow Lava, the Kitts Metagabbro and argillite units; the latter of which forms part of the metasedimentary formation. The argillite unit consists

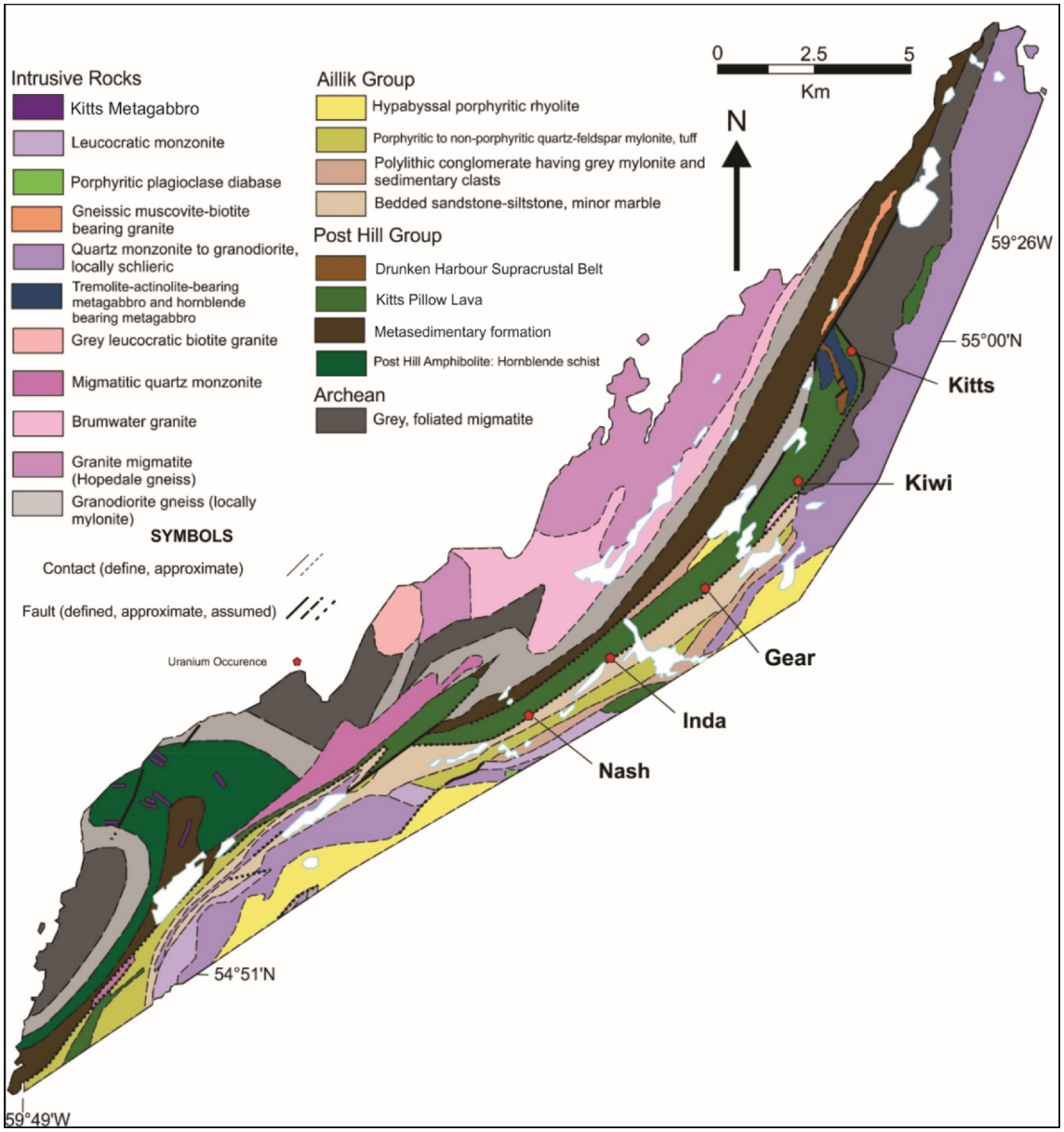


Fig. 2. Geology of the Post Hill group near the Kitts-Post Hill belt, modified from Sparkes (2017).

of multiple beds that have been variably metamorphosed to greenschist-amphibolite facies. Two shear zones were observed in the Kitts deposit by Evans (1980): the northwest-trending Main Shear zone, that is host to uranium mineralization within the argillite and volcaniclastic units, and the north-northeast-trending Cross Shear zone, roughly parallel to regional schistosity, but locally discordant to lithological contacts. Uranium mineralization is generally confined to the argillite unit, along shear zones near the contact with the metagabbro, but minor mineralization also occurs within the Kitts Pillow Lava unit and quartz-feldspar porphyry (Sparkes, 2017). Mineralization seems to be structurally controlled by ductile deformation in the area, as uranium contents have greater than average values where folding is tight (Gandhi, 1978). Mineralization often forms microcrystalline veinlets and/or clots of uraninite rimmed by chlorite, included within amphibole and/or intergrown with calcite, graphite and pyrrhotite.

Mineralization in the Gear (Fig. 3b), Inda (Fig. 3c) and Nash (Fig. 3d) deposits is primarily concentrated within the upper Post Hill Group, near the sheared contact with the adjacent Aillik Group, and mostly within the argillite, metasedimentary and metavolcanic rocks. The footwall of the mineralized zones of these three deposits is largely composed of mafic metavolcanic rocks (Fig. 3). Mineralization at the Gear deposit is confined to the argillite unit where the host rocks are more quartz-rich than at Kitts, Inda or Nash. At the Inda deposit, uranium mineralization is associated with a zone of intercalated felsic and mafic metavolcanic rocks, bounded by the Kitts Pillow Lava unit. Mineralization at the Nash deposit is hosted within the Nakit Shear Zone (Marten, 1977), and is locally hosted within the adjacent ca. 1.8 Ga Aillik Group units. Evans (1980) suggested that the Aillik Group rocks to the west of the Gear, Inda and Nash deposits experienced alkali alteration similar to that seen at the Michelin deposit. Hydrothermal alteration is present throughout the Kitts-Post Hill belt as veins of amphibole, pyroxene, biotite, magnetite and andradite. At the Gear deposit, a Cu-Zn relationship associated with the argillite unit was suggested by Evans (1980) as a possible source for base-metal enrichment. Evans (1980) also suggested a relationship between vanadium and uranium mineralization.

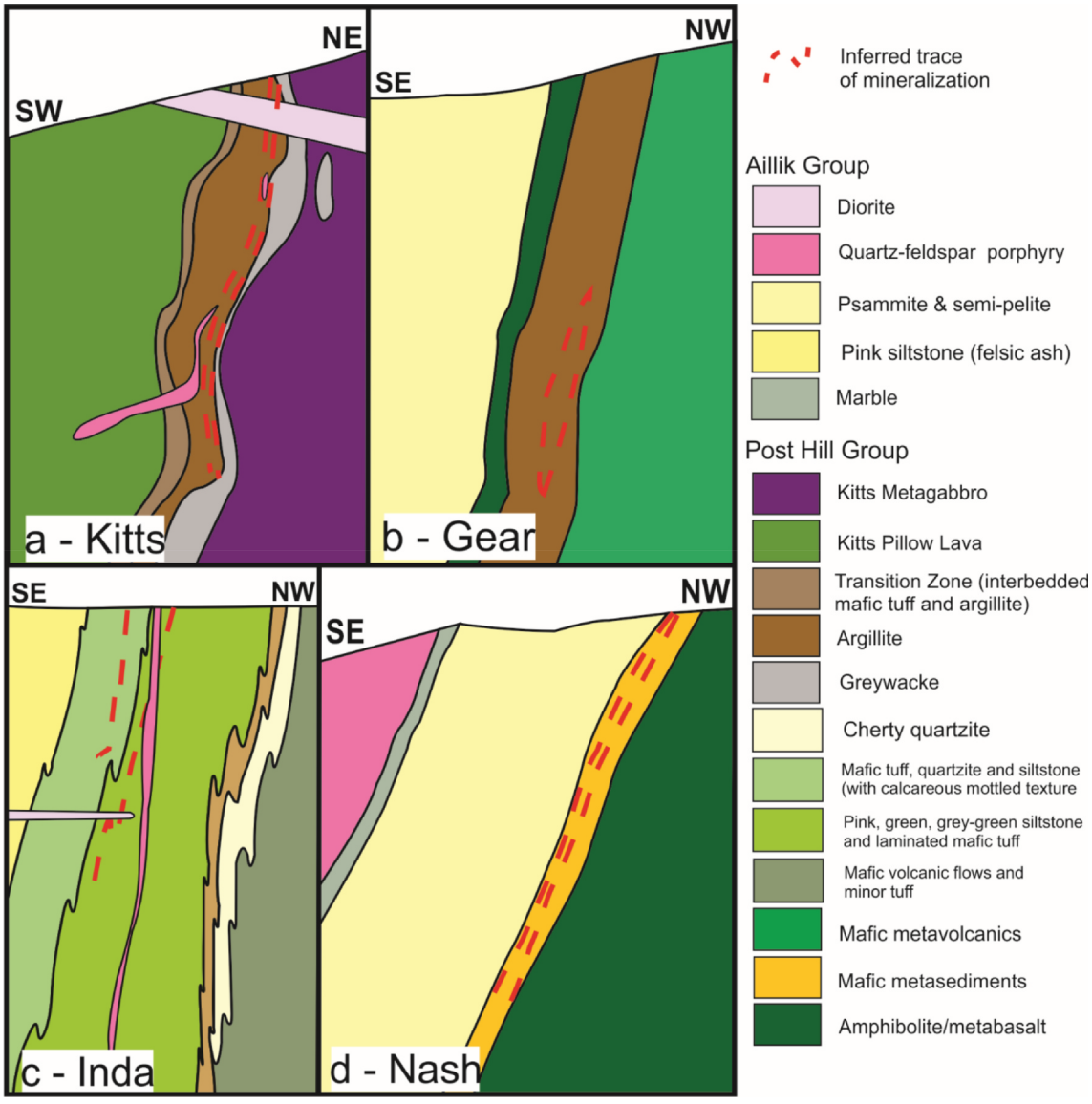


Fig. 3. Simplified cross section of the Kitts-Post Hill deposits: a) Kitts; b) Gear; c) Inda; and d) Nash. Modified from Sparkes (2017).

3.3. Timing of uranium mineralization

The timing of uranium mineralization in the Kitts-Post Hill belt is poorly constrained. Previous work by Gandhi (1978) reported highly variable pitchblende $^{207}Pb/^{206}Pb$ ages for Kitts, Gear and Inda of 1760 Ma, 1990 Ma and 1831 Ma, respectively. Wilton and Longerich (1993) report *in situ* and bulk analyses of uraninite grains and separates via ICP-MS, which yielded two $^{207}Pb/^{206}Pb$ ages of 1777 ± 9 Ma and 1758 ± 3 Ma for the Kitts deposit and an age of 1738 ± 5 Ma for the Inda deposit. Evans (1980) analyzed 24 pitchblende grains from the Kitts deposit by electron microprobe, which yielded a $^{206}Pb/^{238}U$ age of 1785 ± 115 Ma. Using a Sensitive High Resolution Ion Microprobe (SHRIMP), Davis (2002) reported a crystallization age of 1.8 Ga and a probable Pb loss/disturbance event at 450 Ma for the Kitts deposit whereby alteration of uraninite occurred and led to the inclusion of radiogenic Pb in galena. Davis (2002) emphasized the complexities in dating uraninite due to the possibility of post-crystallization alteration effects. In situ analyses of micro-galena crystals associated with the uraninite yielded radiogenic compositions with low $^{208}Pb/^{204}Pb$ ratios, indicating derivation of Pb from a very high U and low Th source at ca. 450 Ma.

Recent geochronological studies by Sparkes et al. (2010) define an older age for mineralization at the Kitts deposit. Analysis of zircon from the pre-mineralization Kitts metagabbro yielded an age of 2018 $^{+15}_{-8}$ Ma, whereas zircon U-Pb SHRIMP analyses from a quartz-feldspar porphyry dyke cross-cutting the mineralization yielded an age of 1881.8 ± 3.4 Ma (Sparkes et al., 2010). Although the dyke contains localized uraninite-filled fractures, these are interpreted to record re-mobilization of uranium from the host rock (Sparkes et al., 2010). The primary mineralization at the Kitts deposit thus likely occurred between 2018 and 1881 Ma, which is much older than the ages obtained by Gandhi (1978), Evans (1980) and Wilton and Longerich (1993). Mineralization at the Nash deposit is also locally hosted by ca. 1860 Ma felsic rocks of the Aillik Group, indicating that at least some of the mineralization at this deposit occurred ≤1860 Ma, which is slightly younger than the age bracket suggested for the Kitts mineralization (Schärer et al., 1988; Sparkes et al., 2010). Uranium showings in the ca. 1802 Ma Long Island quartz monzonite (Kerr et al., 1992) that is in an structural site equivalent to the Kitts Pillow Lava formation, also supports remobilization of uranium after ca. 1860 Ma.

Table 1
Location, drill hole and rock types of the samples examined in this study.

Drill Hole/ Original Sample number	Sample Number (this study)	Deposit	From (m)	To (m)	Host
	18-CD-10	Gear	Surface grab sample		Metavolcanic
	18-CD-16	Inda	Surface grab sample		Metavolcanic
B-49	17-CD-27	Kitts	83.98	84.07	Argillite
GS-08-266	17-CD-68	Kitts	Surface grab sample		Argillite
GS-08-267	17-CD-69	Kitts	Surface grab sample		Argillite
K-74-11	18-CD-14b	Kitts	Surface grab sample		Argillite
G-68-142	17-CD-09	Gear	97.2	97.37	Argillite
NW-77-04	17-CD-18	Nash West	21.05	21.25	Metavolcanic
G-68-135	17-CD-76	Gear	15.41	15.52	Metavolcanic
B-49	17-CD-024	Kitts	81.28	81.39	Argillite
GS-08-268	17-CD-70	Kitts	Surface grab sample		Argillite

4. Methods

4.1. Rock collection and mineral identification

Samples were collected from the Newfoundland and Labrador Geological Survey's core storage facilities in St. John's, Newfoundland and Goose Bay, Labrador. Additional samples were collected from the Sunil S. Gandhi collection housed at the Geological Survey of Canada. The details of samples selected for this study are provided in Tables 1 and 2. Petrographic studies were complemented with scanning electron microscopy to identify the mineralogy and paragenetic relationships.

A Zeiss EVO 50 series scanning electron microscope (SEM) was used to describe the mineralogy of polished thin section samples at the Geological Survey of Canada in Ottawa, Ontario. This system includes a backscattered electron detector (BSE), Everhart-Thornley secondary electron detector (SE), a variable pressure secondary electron detector (VPSE) and a cathodoluminescence detector (CL). The Oxford energy dispersive spectrometry (EDS) system includes the X-MAX 150 silicon drift detector, with INCA Energy 450 software and AZtec Energy 3.1 microanalysis software. The SEM operating conditions were as follows: standard working distance of 8.5 mm; voltage set at 20 kV, with a probe current of 400pA to 1nA; and filament current set to 2nd peak. Images of the samples were acquired using the back scattered electron (BSE) mode. The INCA mineral liberation analysis software was used to find and identify minerals based on chemical composition using EDS.

4.2. Major and trace element geochemistry

4.2.1. Electron probe microanalyzer

Targeted minerals were analyzed for elemental abundances using a JEOL 8230 electron probe microanalyzer (EPMA) at the University of Ottawa. Operating conditions were 20 kV accelerating voltage and 10nA current, with 20 s on peak and 10 s off-peak counting times. A mixture of natural and synthetic pure metal, simple oxides and simple compounds were used as standards. Data were reduced with a ZAF matrix correction using JEOL software. Elements analyzed include: Ca, Ti, Cr, Si, Fe, V, Al, Mg, Mn, K, Cl, Zn, F, Na, Sr, Ba, Ni, Nb, Ce, La, Nd, Y, Pr, U, Th, Pb, Sm, Zr, and P.

4.2.2. In-situ LA-ICP-MS element mapping

Only four samples from the Kitts deposit were used for element mapping given the fine-grained nature (< 5 μm) of uraninite in the Kitts-Post Hill belt sample suite.

Element mapping of uraninite was carried out on selected areas of

Table 2
Representative petrography of alteration and mineralization within the sample suite. Abbreviations: albite (ab) amphibole (amp), andradite (adr), apatite (ap), arsenopyrite (aspy), biotite (bio), calcite (cal), chalcopyrite (cpy), clinozoisite (clz), epidote (ep), galena (gal), hematite (hem), ilmenite (ilm), K-feldspar (K-spar), magnetite (mag), molybdenite (moly), monazite (mnz), pyrite (py), pyroxene (pxn), quartz (qz), titanite (ttn), and uraninite (urn).

Deposit	Sample	Mineralogy	Textures	Grain sizes
Kitts	18-CD-14b	amp, ab, urn, py, aspy, graphite	amp + ab matrix; urn clusters/veins; disseminated py, aspy, graphite	matrix < 500 um; urn < 500 um; py, aspy, graphite < 300 um
	CD-17–67	amp, ab, K-spar, qz, urn, py, graphite	amp + ab + K-spar matrix; qz "pockets"; disseminated py, urn, graphite	silicates < 500 um; urn, graphite < 50 um; py < 1 mm
	CD-17–66	amp, ab, qz, K-spar, ep, urn, py, ttn, ilm, cpy, gal	amp + ab + qz + K-spar + ep matrix; disseminated py; clusters of fine-grained urn, ttn, ilm; py intergrown with cpy (sometimes oxidized); iron veins crosscut urn; secondary urn veins crosscut py	silicates < 100 um; urn, ttn, ilm < 75 um; py < 1 mm
	CD-17–027	amp, ab, K-spar, qz, urn, py, ttn, moly, mnz	ab + amp + K-spar + qz matrix; py veins oriented roughly same direction, disseminated py and ttn, urn, moly, mnz occur in close proximity to amp	silicates < 100 um; urn, ttn, moly < 20 um; py < 1 mm; mnz < 100 um
Inda	18-CD-16	amp, ab, mag, hem, cal, ttn, urn	amp + ab matrix; disseminated FeO, cal, ttn, urn	all grains < 100 um
Gear	18-CD-10	mag, hem, Ca-amp, ab, urn, qz, ap	lamellae of FeO and amp + ab; disseminated urn and lamellae of urn; minor qz in matrix, ap assc. with hem	mag, hem, amp, ab, qz < 100 um; urn < 20 um; ap < 50 um
	17-CD-09	pxn, amp, adr, ab, py, REE	pxn + minor amp with wavey lamellae of adr in one half of section; amp with minor pxn in other half; clusters of plag and disseminate py; veins of plag seem crosscut by pxn; REE ore mineralization assc. with plag in adr lamellae	silicates < 1 mm; disseminated py < 1 mm (single grain > 1 cm); REE < 50 um
	17-CD-76	bio, amp, K-spar, cal, ab, mag, ttn	high altered; lamellae of bio + amp + minor K-spar + cal; matrix of K-spar, bio, ab, amp, mag, ttn	lamellae grains < 1 mm; matrix K-spar, bio, plag < 100 um; matrix amp, mag, ttn < 1 mm
Nash W	17-CD-18	amp, K-spar, cal, amp, ab, clz, mag	alternating layers of amp, K-spar, cal; amp, ab, minor clz and K-spar; clz and mag	all grains < 1 mm; mag and clz layer < 2 mm

either thin or thick (~200 μm) sections by laser ablation inductively coupled plasma mass spectrometry (LA-ICP-MS) at the Geological Survey of Canada, using a Photon Machines Analyte G2 193 excimer laser ablation system, with a Helex II ablation cell, coupled to an Agilent 7700x quadrupole ICP-MS. The mapping procedure closely follows the method of Lawley et al. (2015, 2020) and Paradis et al. (2020). Element maps were constructed by rastering a focused laser beam across the sample surface to form a series of line scans. Laser conditions during the analytical sessions include: a fluence of 4.3–4.9 J/cm^2, a repetition rate of 30 Hz, a spot size of 5 μm, and a scan speed of 5 μm/s. Prior to each ablation pass, the sample surface was cleaned by rastering the laser across the sample at a rate of 2–3 pulses every 5 μm, and was then followed by 50–60 s of washout. Each analysis began with 20 s of background measurement (gas blank). The ablation aerosol was transported out of the Helex II cell using 1 L/min of helium gas, and was subsequently mixed with ~1 L/min of argon gas before entering the ICP-MS. The ICP-MS was tuned on NIST-612 to achieve > 9000 cps/ppm on ^{175}Lu (50 μm spot, ~7 J/cm2 at 10 Hz), while minimizing the production of oxides (< 0.2% for ThO/Th) and maintaining a U/Th ratio of ~1.0. The total duty cycle time to measure all masses on the ICP-MS (in time-resolved analysis mode) was 250 ms. Utilizing these settings, every 1 s of analysis or the equivalent of a 5 μm spot diameter, included four full scans of the mass spectrometer.

The calibration procedures of Jackson (2008a) were followed during the mapping sessions. Standardization was achieved by calibrating the signals of unknowns against analyses of GSE-1G (for most major and trace elements), and internal reference materials pyrrhotite (sulphur calibration) and calcite (carbon calibration), and normalizing total element (or element oxide) concentrations to 100%. Reference materials were analyzed every 20 unknowns to account for instrument drift during the mapping run. Line scans of secondary standards GSD-1G or NIST-610 were analyzed throughout the mapping sessions, and routinely yielded calculated concentrations within 5–10% of the accepted values for most elements. Reference values for GSE-1G, GSD-1G and NIST-610 were taken from the online geological and environmental reference materials database (GeoReM; Jochum et al., 2005). The software programs LAMTRACE and PixeLAte (Jackson, 2008b) were used to calibrate the data and convert the line scans to quantitative elemental maps. Elements analyzed include: Na, Mg, Al, Si, P, S, K, Ca, Ti, V, Cr, Mn, Fe, Co, Ni, Cu, Zn, As, Sr, Y, Zr, Nb, Mo, Cs, Ba, La, Ce, Pr, Nd, Sm, Eu, Gd, Tb, Dy, Ho, Er, Tm, Yb, Lu, Hf, Ta, W, Tl, ^{206}Pb, ^{207}Pb, ^{208}Pb, Bi, Th, ^{235}U, and ^{238}U. Raw count rates for the individual Pb isotopes were summed prior to calibration, such that a Total Pb concentration could be calculated. The concentration for each of the three individual Pb isotopes was determined by comparing against the isotopic abundance of Pb in GSE-1G. A uraninite grain from the Mistamisk deposit was also analyzed by *in-situ* LA-ICP-MS as an external standard (composition reported by Lach et al., 2013) and for comparison with the Kitts uraninite. The data are presented in Table 6.

Chondrite normalized rare earth element patterns were produced from the LA-ICP-MS maps by extracting data for individual pixels associated with uraninite (normalized to values reported in McDonough and Sun, 1995). Uraninite was classified against altered and mixed analyses (i.e., ablation of two or more minerals) by discarding pixels that had < 70 wt% UO_2, > 1.5 wt% SiO_2 and > 1 wt% CaO.

5. Results

5.1. Petrography

The generalized paragenetic sequence for the Post Hill trend sample suite is shown in Figure 4. General sample information is given in Table 1, whereas Table 2, Figures 5 and 6 present textural relations of key minerals from selected samples. Uranium mineralization consists mainly fine-grained uraninite that is variably (minor to completely) altered to coffinite. Associated ore minerals include molybdenite, pyrite, chalcopyrite, aresenopyrite, galena, scheelite, Ni-Co-Zn sulfides, and Ti-oxides (Fig. 4).

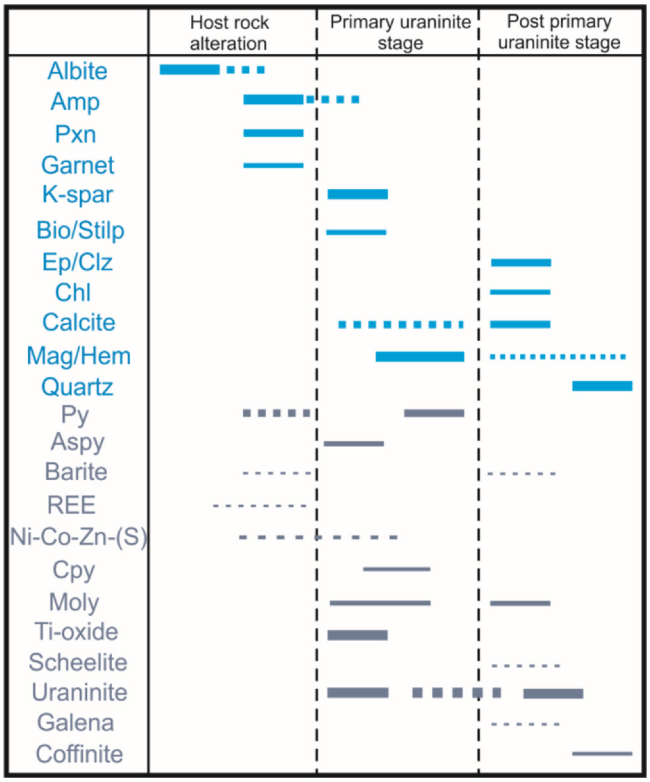


Fig. 4. Generalized paragenetic sequence of the deposits within the Kitts-Post Hill trend, weight of lines indicate relative abundance, dashed lines represent uncertainty in the sequence. Abbreviations: amphibole (amp), arsenopyrite (aspy), biotite (bio), chalcopyrite (cpy).chlorite (chl), clinozoisite (clz), epidote (ep), hematite (hem), K-feldspar (K-spar), magnetite (mag), molybdenite (moly), pyrite (py), pyroxene (pxn) and, stilpnomelane (stilp).

Sodic alteration in the sample suite is pervasive and occurs as the earliest alteration event in the form of porous, fine-grained albite matrix. The porosity within albite hosts REE mineralization (of an unidentifiable mineral) in some samples (Fig. 6c). Electron probe microanalyses of amphibole from throughout the suite yield magnesio-hornblende, ferro-hornblende, magnesio-ferri-hornblende and hastingsite compositions (Table 3) using the Locock (2014) classification. Fine-grained amphibole and veins of fine-to coarse-grained amphibole locally crosscut albite. Disseminated uraninite occurs as inclusions within amphibole, but is more often observed around the margins of amphibole grains or veins (Fig. 5f). Less commonly, the amphibole and uraninite also occur intergrown with magnetite (Fig. 5a).

Some skarn-like alteration is observed at the Gear deposit, and may be present in the Nash West deposit. The Ca-Fe skarn-like alteration occurs in the Gear deposit as pervasive hedenbergite pyroxene and andradite garnet, and locally overprints albite (Fig. 6a). Andradite occurs as veinlets rimmed by fine-grained albite in a matrix of K-feldspar at the Nash deposit, which may represent a skarn-like alteration phase (Fig. 6e).

Very fine-grained (< 10 μm) K-feldspar inclusions in albite create a myrmekitic-like texture and occur syn-genetically with uraninite in veinlets cutting the Na-alteration assemblage (Fig. 5e). Veinlets of fine-grained K-feldspar, calcite and minor amphibole are crosscut by veins of clinozoisite and magnetite (Fig. 6b). A veinlet of stilpnomelane was observed in sample GS-08-268 from the Kitts deposit, crosscutting albite (Fig. 6d). Stilpnomelane in spatial association with uraninite was observed in a sample from the Kitts deposit (Fig. 5c).

Uraninite textures throughout the sample suite are variable,

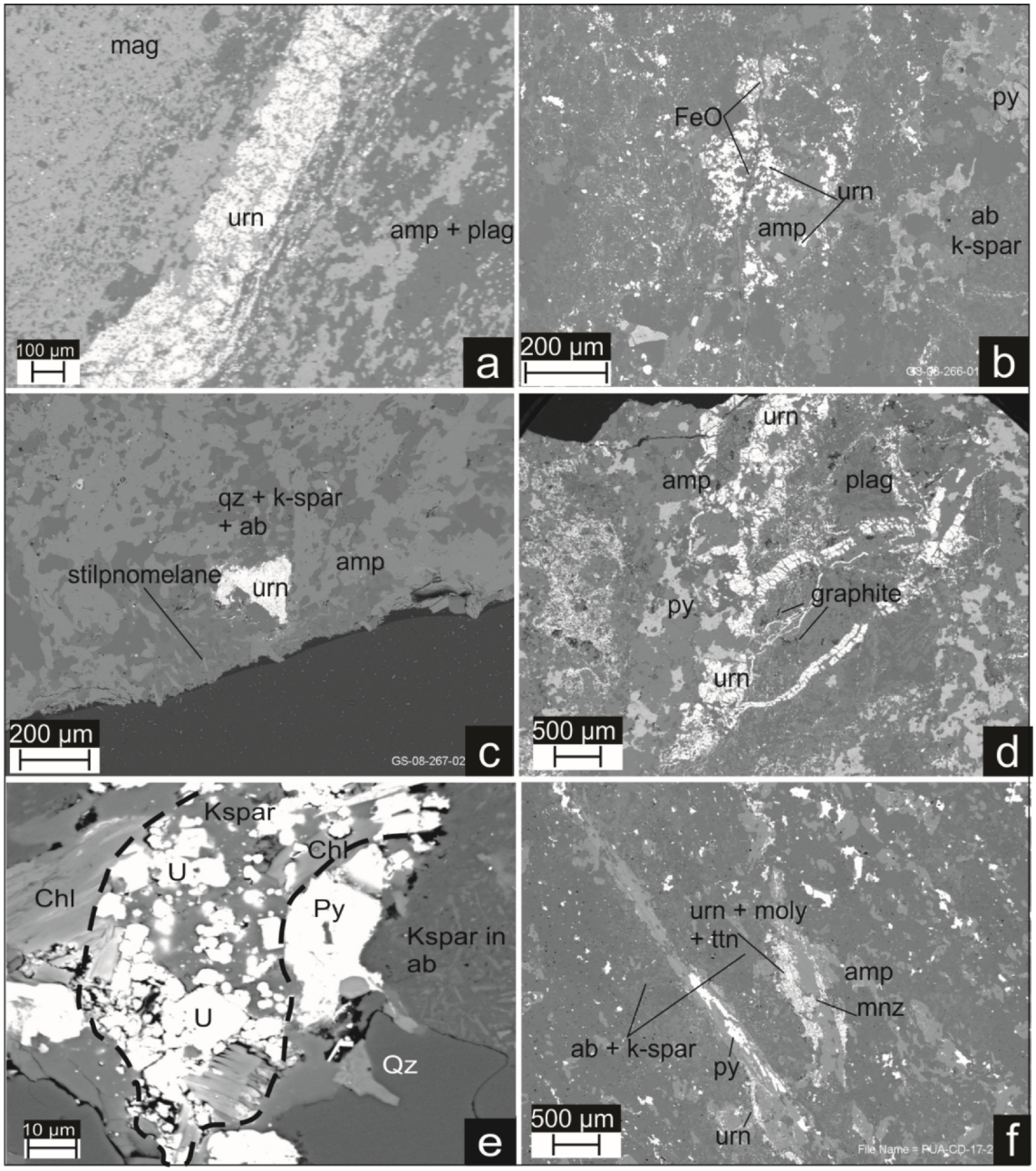


Fig. 5. Backscatter electron (BSE) images of (a) fine-grained uraninite in veinlet cutting albite, amphibole and magnetite; sample 18-CD-10. (b) Fine-grained uraninite in amphibole, plagioclase and K-feldspar crosscut by late iron oxide veinlet; sample GS-08-266. (c) Uraninite in amphibole, plagioclase, quartz, K-feldspar and stilpnomelane; sample GS-08-267, (d) Coarse-grained uraninite veinlet crosscutting plagioclase and amphibole; sample 18-CD-14b. (e) Fine-grained uraninite in matrix of K-feldspar and chlorite; sample 17-CD-024. (f) Fine-grained amphibole veinlet crosscutting plagioclase, rimmed by fine-grained uraninite, molybdenite, titanite and monzonite; sample CD-17-027. Abbreviations: amphibole (amp), arsenopyrite (aspy), biotite (bio), chalcopyrite (cpy).chlorite (chl), clinozoisite (clz), epidote (ep), hematite (hem), K-feldspar (K-spar), magnetite (mag), molybdenite (moly), pyrite (py), pyroxene (pxn) and, stilpnomelane (stilp).

including fine-grained disseminations, fine-grained clusters, veinlets and fine-grained folded bands. All textural varieties occur within a Ca-Fe alteration assemblage (amphibole and magnetite) in spatial or genetic association with K-feldspar and locally overprint magnetite (K-Fe alteration). Uraninite grains of Sample 18-CD-14b are the coarsest-grained of the sample suite (50–100 µm diameter) and occur in "clusters" and in vein-like structures (Fig. 5d). Uraninite grains of Sample GS-08-266 are on average 20 µm in diameter and occur in "clusters" of grains, crosscut by iron oxide veins (Fig. 5b). Uraninite grains of Sample GS-08-267 are very fine-grained (< 20 um diameter) and occur in "clusters" and a vein-like structure (Fig. 5c). Uraninite grains of Sample 17-CD-027 are very fine-grained (< 20 µm diameter) and occur as disseminated in a vein-like structure (Fig. 5f).

5.2. Uraninite electron probe microanalyzer data

Uraninite EPMA data are summarized in Table 4, where they are subdivided into three groups, for which average compositions are also reported. Overall the major to minor element concentrations are similar but with slight variations in CaO, La_2O_3, Nd_2O_3, Fe_2O_3, ThO_2, and Y_2O_3 contents. Between the groups, UO_2 contents varied slightly from a high of 78.23 wt% in Group 1 to a low of 73.37 wt% in Group 3, whereas PbO contents ranged from 21.54 wt% (Group 1) to 19.83 wt% (group 3). Slight variations in U/Pb ratios were observed between the three

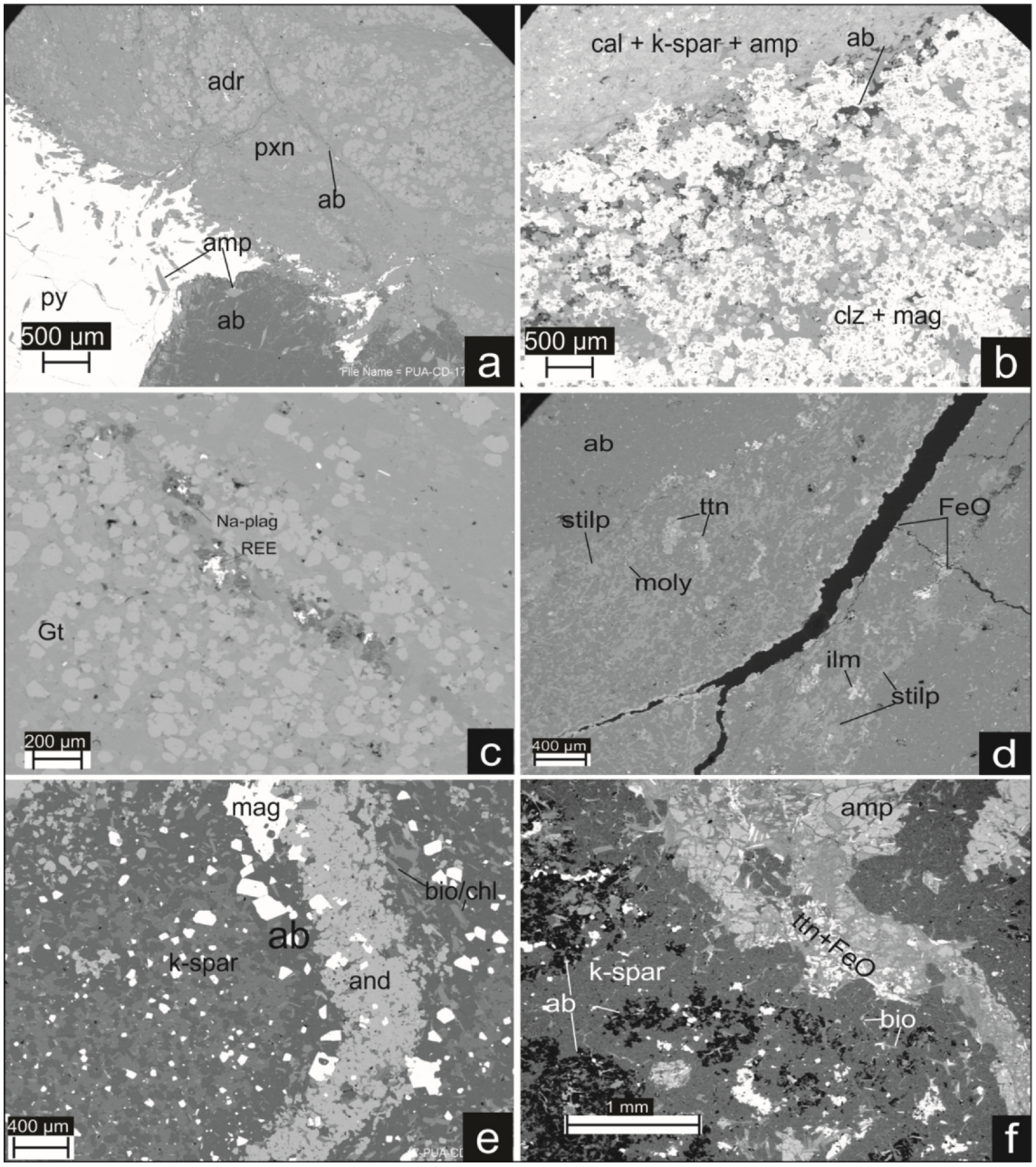


Fig. 6. BSE images of (a) coarse-grained pyrite with inclusions of amphibole in matrix of albite, juxtaposed against a matrix of pyroxene and andradite, which is being cross-cut by veinlet of fine-grained albite; Sample 17-CD-09. (b) Clinozoisite and magnetite veinlet crosscutting matrix of albite, amphibole, K-feldspar and calcite; Sample 17-CD-17. (c) Amphibole and garnet matrix hosting an albite veinlet, that is host to fine-grained REE mineralization; Sample 17-CD-09. (d) Veinlet of fine-grained stilpnomelane with minor molybdenite, titanite and ilmenite crosscutting albite matrix; Sample GS-08-268. (e) Fine-grained andradite veinlet crosscutting albite, biotite/chlorite and K-feldspar, overprinted by magnetite; Sample 17-CD-10. (f) Coarse-grained amphibole-titanite-iron-oxide veinlet crosscutting albite, K-feldspar and biotite matrix; Sample 17-CD-76. Abbreviations: amphibole (amp), arsenopyrite (aspy), biotite (bio), chalcopyrite (cpy).chlorite (chl), clinozoisite (clz), epidote (ep), hematite (hem), K-feldspar (K-spar), magnetite (mag), molybdenite (moly), pyrite (py), pyroxene (pxn) and, stilpnomelane (stilp).

groups; Group 2 had the highest U/Pb ratios with an average value of 3.15, and Group 1 and 3 had similar ratios with averages of 3.01 and 3.07 respectively. Chemical U-Pb ages of the uraninite grains analyzed by EPMA were determined using the Bowles (2015) method. The calculated chemical ages range from 1360 to 1880 Ma (Duffett, 2019), but these data are not discussed in detail given the large uncertainties of the method on uraninite grains that have ages > 1000 Ma (Bowles, 2015).

5.3. Uraninite LA-ICP-MS data

As documented by several authors (e.g. Cuney, 2010; Fayek and Kyser, 1997; Fryer and Taylor, 1987; Hidaka et al., 1992; Hidaka and Gauthier-Lafaye, 2001; Maas and McCulloch, 1990; Pagel et al., 1987; Mercadier et al., 2011; Frimmel et al., 2014), the trace element chemistry of uraninite reflects the conditions under which the mineral crystallized (combination of fluid chemistry, temperature, source materials, etc.) and chondrite-normalized plots reveal distinct REE patterns for certain ore deposit types (e.g. Mercadier et al., 2011; Frimmel et al., 2014).

Samples from the Kitts deposit contained uraninite grains that were large enough (> 20 µm) to be analyzed accurately by LA-ICP-MS, whereas uraninite from other deposits proved to be too fine-grained

Table 3
. Electron microprobe analyses of silicate minerals in uranium occurrences, data in wt % (* denotes average composition).

	AMPHIBOLE										CHL	ALBITE	K-SPAR	PXN
	*17-CD-027	σ	*18-CD-10	σ	*GS-08–267-01	σ	GS-08–267-03	DL	*GS-08–266-01b	σ	17-CD-024	17-CD-024	17-CD-024	17-CD-008
CaO	11.67	0.03	10.85	0.06	11.72	0.07	11.66	0.02	11.43	0.06	1.82	2.15	0.15	22.99
TiO_2	0.33	0.01	0.32	0.02	0.82	0.03	0.81	0.02	0.62	0.03	1.04	–	–	–
Cr_2O_3	0.21	0.01	–	0.01	–		–	0.02	0.09	0.01	0.24	–	–	–
SiO_2	49.75	0.27	39.5	0.35	43.13	0.44	42.59	0.03	45.92	0.54	27.33	63.04	64.19	51.07
FeO	13.21	0.24	19.85	0.39	20.88	0.1	20.63	0.04	18.26	0.09	24.24	0.65	0.67	18.35
V_2O_3	0.32	0.09	0.94	0.04	0.08	0.03	0.16	0.04	0.12	0.02	0.14	–	–	–
Al_2O_3	5.82	0.01	12.94	0.19	12.45	0.31	12.17	0.02	9.36	0.17	16.88	22.33	18.49	0.31
MgO	14.36	0.07	8.23	0.15	6.62	0.25	6.78	0.02	9.4	0.24	6.92	0.1	–	6.69
MnO	0.49	0.02	0.84	0.01	0.31	0.03	0.36	0.03	0.49	0.03	1.65	–	–	1.16
K_2O	0.14	0.02	0.49	0.03	0.9	0.02	0.9	0.02	0.38	0.03	0.06	1.24	15.1	–
Cl	–		–	–	0.05	0.01	0.05	0.01	0.06	0.01	0.16	–	–	–
ZnO	–		–	0.05	0.06	0.05	0.06	0.1	0.08	0.02	0.25	–	0.05	0.09
F	0.12	0.01	–	0.12	0.18	0.14	0.23	0.21	0.15	0.08	0.07	–	–	–
Na_2O	0.69	0.03	2.8	0.06	1.03	0.05	1.07	0.03	0.85	0.05	0.12	10.05	0.16	0.25
SrO	0.08	0.02	0.11	0.02	0.07	0.02	0.09	0.04	0.11	0.01	–	0.18	–	0.1
BaO	–		–	0.02	–		–	0.04	–		–	–	0.33	–
NiO	–		–	–	–		–	0.04	–		–	–	–	–
Nb_2O_5	–		–	0.05	–		–	0.11	–		–	–	–	–
TOTAL	97.19		96.87		98.3		97.56		97.32		80.98	99.91	99.2	101.26

Table 4
Electron microprobe analyses of average uraninite compositions in uranium occurrences, data in in wt%

	Group 1								Group 2							
	18-CD-14a						18-CD-14b		GS-08–266							
	1	σ	2	σ	3	σ	1	σ	1a	σ	1b	σ	1c	σ	2	σ
SiO_2	0.18	0.13	0.2	0.24	0.1	0.03	0.32	0.21	0.1	0.07	0.15	0.07	0.17	0.1	0.15	0.13
UO_2	78.23	2.06	77.82	0.69	77.02	1.12	77.84	1.06	77.07	0.87	76.8	0.87	77.16	0.98	76.63	1.01
PbO	21.45	0.75	21.54	0.41	21.18	0.37	21.37	0.3	20.35	0.59	20	0.59	20.13	0.78	20.44	0.9
CaO	0.39	0.17	0.31	0.06	0.32	0.04	0.48	0.08	0.25	0.08	0.31	0.08	0.3	0.16	0.24	0.08
La_2O_3	0.1	0.07	0.08	0.13	0.07	0.11	0.06	0.06	0.07	0.08	0.07	0.08	–	0.07	0.08	0.12
Ce_2O_3	0.12	0.09	0.15	0.07	0.13	0.09	0.05	0.05	0.1	0.09	0.1	0.09	0.09	0.1	0.13	0.11
Nd_2O_3	0.24	0.13	0.31	0.07	0.27	0.08	0.16	0.1	0.18	0.1	0.17	0.1	0.16	0.1	0.17	0.1
Sm_2O_3	–	0.03	0.04	0.05	–	0.02	0.04	0.03	0.05	0.05	–	0.05	0.05	0.05	0.05	0.06
FeO	0.15	0.2	–	0.02	0.09	0.07	0.08	0.05	0.19	0.14	0.2	0.14	0.16	0.16	0.23	0.18
ThO_2	0.05	0.05	0.11	0.08	–	0.04	0.06	0.06	0.05	0.05	–	0.05	0.06	0.06	0.09	0.07
P_2O_5	–	0.02	–	0.03	0.01	0.02	–	0	–	0.02	–	0.02	–	0.02	–	0.01
Y_2O_3	0.11	0.03	0.12	0.04	0.11	0.04	0.1	0.05	0.2	0.06	0.18	0.06	0.17	0.07	0.27	0.08
ZrO_2	0.08	0.16	–	0.03	–	0.03	–	0.04	0.05	0.07	–	0.07	–	0.05	0.27	0.94
Total	101.01		100.66		99.3		100.37		98.62		97.97		98.43		98.68	

	Group 3						Group 3				Group 1		Group 2		Group 3	
	17-CD-025		17-CD-027		17-CD-024		GS-08–267				mean	std. dev	mean	std. dev	mean	std. dev
		σ		σ		σ	1	σ	3	σ						
SiO_2	0.33	0.25	0.09	0.27	–	0.04	0.11	0.06	0.11	0.04	0.18	0.17	0.13	0.12	0.11	0.16
UO_2	73.37	2.44	73.86	1.18	73.66	1.13	76.78	1.83	75.17	0.73	77.76	1.57	76.98	0.96	75.31	2.00
PbO	20.28	0.6	20.48	0.5	20.67	0.53	20.42	1.86	19.83	0.58	21.38	0.57	20.24	0.70	20.34	1.29
CaO	0.24	0.15	0.23	0.13	0.08	0.04	0.33	0.21	0.26	0.09	0.36	0.13	0.27	0.13	0.27	0.17
La_2O_3	–	0.06	0.08	0.11	0.16	0.15	0.06	0.09	–	0.05	0.08	0.10	0.06	0.09	0.06	0.10
Ce_2O_3	0.18	0.1	0.09	0.09	0.14	0.06	0.11	0.1	0.08	0.06	0.12	0.09	0.10	0.10	0.10	0.09
Nd_2O_3	0.18	0.17	0.17	0.1	0.17	0.12	0.18	0.09	0.19	0.09	0.25	0.11	0.17	0.10	0.18	0.10
Sm_2O_3	0.11	0.06	0.13	0.09	0.1	0.07	0.05	0.05	–	0.06	0.02	0.03	0.05	0.05	0.08	0.08
FeO	0.9	0.46	0.31	0.18	0.54	0.21	0.45	0.18	0.07	0.03	0.10	0.14	0.19	0.15	0.37	0.28
ThO_2	0.85	0.2	0.06	0.05	2.24	0.18	0.05	0.05	–	0.02	0.06	0.06	0.05	0.06	0.28	0.65
P_2O_5	–	0	–	0	–	0	0.01	0.02	–	0.03	0.02	0.03	0.01	0.02	0.01	0.02
Y_2O_3	0.74	0.12	1.78	0.55	1.23	0.12	0.18	0.11	0.32	0.07	0.11	0.04	0.20	0.08	0.71	0.72
ZrO_2	0.66	0.85	0.15	0.13	–	0.03	–	0.04	0.05	0.04	0.05	0.10	0.07	0.36	0.10	0.27
Total	97.88		95.92		99.05		98.72		96.12							

and/or altered for such analyses. Analyses of uraninite from the Kitts deposit revealed three distinct populations, which are defined by chondrite-normalized REE patterns (Fig. 7). Three different groups were defined on the basis of their overall shapes and light- to heavy-REE ratios (LREE/HREE). Group 1 uraninite grains were noted from sample 18-CD-14b and yield relatively flat patterns with slight depletions in La, and a median LREE/HREE value of 0.99. Group 2 uraninite analyses, represented by sample GS-08-266, have slight enrichments in the middle REE that create slight bell- or convex-shaped patterns, positive europium anomalies and a median LREE/HREE value of 1.08.

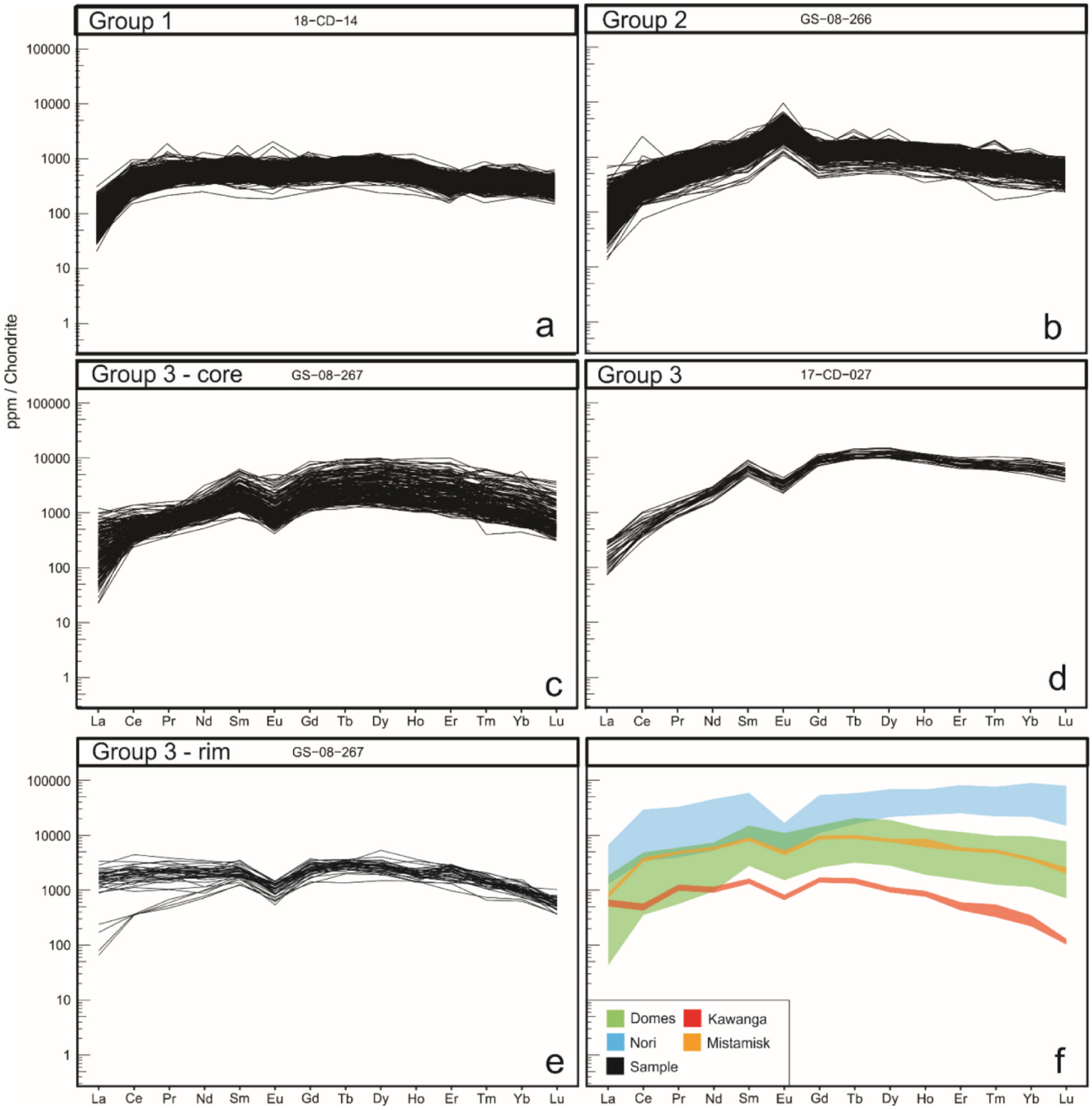


Fig. 7. Chondrite normalized REE plots for uraninite from the Kitts deposit (black lines), plotted against data from the Mistamisk veins of Quebec (orange lines, this study), Nori deposit of the Great Bear magmatic zone (blue lines, Potter et al., 2014, in press), Kawanga deposit of Zambia (red lines, Mercadier et al., 2011), and Domes region of Zambia respectively (green lines, Eglinger et al., 2013). (For interpretation of the references to colour in this figure legend, the reader is referred to the web version of this article.)

Group 3 uraninite grains from samples GS-08-267 and 17-CD-027, have lop-sided bell-shaped patterns with lower La–Nd values, negative europium anomalies and a median LREE/HREE value of 0.58. Representative LA-ICP-MS trace element data of uraninite are given in Table 5. Figures 8–11 provide a visual representation of the spatial geochemical variation in uraninite grains from the Kitts deposit.

Overall REE abundances of Group 1 are the lowest of all three populations, with a median value for the sum of REEs of 0.12 wt%. The U/Th ratio varies from 1054 to 11332, with a median value of 2889, corresponding with the highest values of the dataset (Table 5). Group 1 uraninites are variably altered, as revealed by the slight decrease in uranium contents along grain margins and a decrease in Th from a maximum value of 1680 ppm to a minimum of 87 ppm (Fig. 8f). Slight UO_2 and La enrichment of about 0.5 wt% and 2 ppm, respectively, occur along grain boundaries (Fig. 8b,e). Localized enrichments in zirconium, likely in the form of clusters or inclusions within the uraninite grains, is visible in Figure 8d.

Group 2 has the second lowest REE chondrite normalized abundances overall (Fig. 7b), with a median value of ΣREEs = 0.21 wt%. Heavy REE are enriched relative to LREE, but the former have relatively flat profiles, and higher concentrations relative to those of Group 1. The LREE are enriched from La through Eu and a strong positive europium anomaly occurs only in sample GS-08-266. Lanthanum abundances are low compared to all other elements. The U/Th ratios vary between 412 and 3593, with a median value of 1229 (Table 5). Group 2 uraninite is enriched in Zr (up to 30 000 ppm), and slightly enriched in W (up to

Table 5
Representative median concentrations for the trace element data of uraninite from LA-ICP-MS (in ppm), including detection limits (LLD). Top row is the sample number, second row gives the location number analyzed on the sample.

	18-CD-14b				GS-08–266				GS-08–267				17-CD-027			
	1	LLD	2	LLD	1	LLD	2	LLD	1	LLD	2	LLD		LLD		LLD
Y	1009	0.018	1287	0.002	1646	0.038	1442	0.029	2414	0.045	2077	0.036	15,563	0.036	15,283	0.036
Zr	1708	0.035	6792	0.002	5598	0.075	4504	0.065	669	0.093	127	0.097	1436	0.052	2005	0.052
Nb	1.71	0.021	3.53	0.005	51.2	0.33	6.25	0.03	0.054	0.054	5.22	0.048	24.4	0.028	21.4	0.028
Cs	–	–	–	–	–	–	–	–	–	–	–	–	140	0.231	1423	0.231
Ba	0.175	0.175	6.75	0.061	7.86	0.213	12.3	0.222	0.286	0.286	40.3	0.278	13.2	0.246	23.7	0.246
La	13.5	0.011	16.8	0.015	35.9	0.028	21.9	0.032	23	0.031	233	0.029	19.4	0.029	73.8	0.029
Ce	169	0	194	0.006	186	0.021	151	0.027	267	0.039	847	0.026	233	0.028	384	0.028
Pr	43	0.013	43.9	0.003	51.6	0.015	36.1	0.02	62.9	0.027	151	0.022	81.2	0.02	114	0.02
Nd	261	0	338	0.035	297	0.152	340	0.124	644	0.167	826	0.123	883	0.085	1144	0.085
Sm	84	0.042	141	0.038	160	0.1	149	0.132	406	0.189	236	0.123	850	0.147	911	0.147
Eu	32.7	0.013	52.9	0.018	160	0.042	154	0.042	51.7	0.065	48.3	0.041	152	0.037	183	0.037
Gd	128	0.121	183	0.103	248	0.147	208	0.187	513	0.205	373	0.176	1602	0.191	1740	0.191
Tb	20.8	0.015	30.3	0.014	50.2	0.023	45	0.016	107	0.022	97.8	0.026	378	0.02	360	0.02
Dy	150	0.052	265	0.028	334	0.081	297	0.05	766	0.145	548	0.117	2457	0.09	2634	0.09
Ho	31	0.018	31.5	0.015	48.7	0.019	56.3	0.023	145	0.035	112	0.031	445	0.028	550	0.028
Er	54.3	0.016	76.7	0.046	142	0.087	153	0.085	269	0.09	309	0.161	1046	0.086	1250	0.086
Tm	9.05	0.006	12	0.007	15.7	0.014	16.2	0.014	30.5	0.023	35.2	0.028	159	0.019	184	0.019
Yb	63.9	0.127	91.3	0.064	112	0.13	114	0.105	140	0.174	126	0.152	961	0.152	954	0.152
Lu	8.1	0.022	12.8	0.019	10.1	0.023	15.2	0.017	15	0.034	11.4	0.031	104	0.023	117	0.023
Hf	7.87	0.057	29.8	0.062	26.1	0.069	26.7	0.066	2.81	0.103	0.931	0.096	10.2	0.089	16.8	0.089
Ta	0.023	0.023	0.011	0.011	2.1	0.024	0.116	0.023	0.253	0.03	0.738	0.022	2.49	0.023	2.92	0.023
Bi	2.09	0.052	4.22	0.041	3.16	0.072	4.89	0.069	1.36	0.084	0.992	0.063	1.84	0.06	9.12	0.06
Th	220	0.024	375	0.023	479	0.032	599	0.037	608	0.039	126	0.038	1073	0.036	1058	0.036
LREE/HREE avg	1.1459		0.9711		0.6518		0.6593		0.6886		1.3807		0.2829		0.3295	
U/Th avg	2362				1214		1313		1230		6196		617			
REE (La-Lu) sum	1068.4		1489.2		1851.2		1756.7		3440.1		3953.7		9370.6		10,599	

Table 6
Average REE contents of Mistamisk uraninite compared to analyses by Lach et al. (2013). Analyses by LA-ICP-MS in this study, with uncertainties reported as 1 standard deviation (σ).

	This study (n = 39)		Lach et al. (2013) (n = 40)	
	AVG	σ	AVG	σ
La	279	42	275	68
Ce	2981	278	2783	488
Pr	620	55	520	78
Nd	3937	359	3266	494
Sm	1790	201	1393	183
Eu	348	49	266	39
Gd	1710	233	1380	195
Tb	336	48	285	45
Dy	2294	346	1918	336
Ho	405	62	335	55
Er	889	153	850	141
Tm	117	19	89	14
Yb	640	102	490	79
Lu	54	9	44	7

290 ppm). A late iron oxide vein, enriched in W (up to 1330 ppm), Mo (up to 280 ppm), and Ni (up to 250 ppm), crosscuts the uraninite grains (Fig. 5b).

Group 3 has the highest REE abundances overall (Fig. 7c–e) with a median value for ΣREE of 0.38 wt%. Heavy rare earth elements are enriched relative to LREE, decreasing in abundance from Dy through Lu, and a LREE increase from La to Sm, resulting in a pseudo-bell shaped pattern with a strong negative europium anomaly. Lanthanum is depleted relative to all the other REE. The U/Th ratios span from 438 to 17,656 and have a median value of 1413 (Table 5). Group 3 uraninite is enriched in Zr (up to 5500 ppm), Mo (up to 8100 ppm) and Nb (up to 46 ppm) and are enriched in Zr, La and Mo in the rim (Figs. 10e, f, g, 9d). A U, La and ^{206}Pb enrichment of 0.2 wt%, 30 ppm and 10 000 ppm, respectively, is present along fractures and grain boundaries trending away from the uraninite (Fig. 10b, c, g), whereas HREE contents (e.g., Lu; Fig. 10h) remain uniformly distributed in the uraninite. Remobilization of uranium is visible along fractures within the amphibole grain (Fig. 11b).

In the trace element maps, most uraninite grains record leaching of U, Pb and La (Figs. 9–11 of Groups 1 and 3) along fractures indicating remobilization of some elements from the crystals. The trace element maps for sample GS-08–267 (Figs. 9 and 10) also indicate the presence of primary uraninite with an altered rim. The uraninite rim is enriched in La, Mo and Zr relative to the cores, with up to 3363 ppm La, 386 ppm Mo and 611 ppm Zr (median of 183 ppm) in the rim compared to 2278 ppm La, 87 ppm Mo and 6831 ppm Zr (median of 74 ppm) in the core (Fig. 7c, e).

6. Discussion

6.1. IOAA facies in the Kitts-Post Hill belt

Despite the poor constraints on the timing of mineralization and the varied views on metallogenic processes in the Kitts-Post Hill belt (Gandhi, 1978; Evans, 1980; Wilton and Wardle, 1987; Wilton and Longerich, 1993), a metasomatic-hydrothermal origin is implied by the association of uranium mineralization with alkali-calcic and iron metasomatism, metamorphic-metasomatic minerals, elevated Th and REE contents in some generations of uraninite and correlations between uranium and zirconium contents (Evans, 1980; Sparkes and Kerr, 2008; this study). However, there remains a knowledge gap concerning the spatial and temporal connections between uranium occurrences in the Kitts-Post Hill belt and those of other mineralized areas in the CMB. There is also a lack of comparative analyses between these deposits and possibly analogous uranium deposits elsewhere in the world. This final section of the paper makes an attempt to address these deficiencies.

The presence of uraninite inclusions within amphibole and cross-cutting, vein-like zones containing uraninite noted in this study are in agreement with previous work of Evans (1980), and Marten (1977), who proposed that uranium mineralization was linked to formation of amphibole and was structurally controlled. Our detailed inspection of

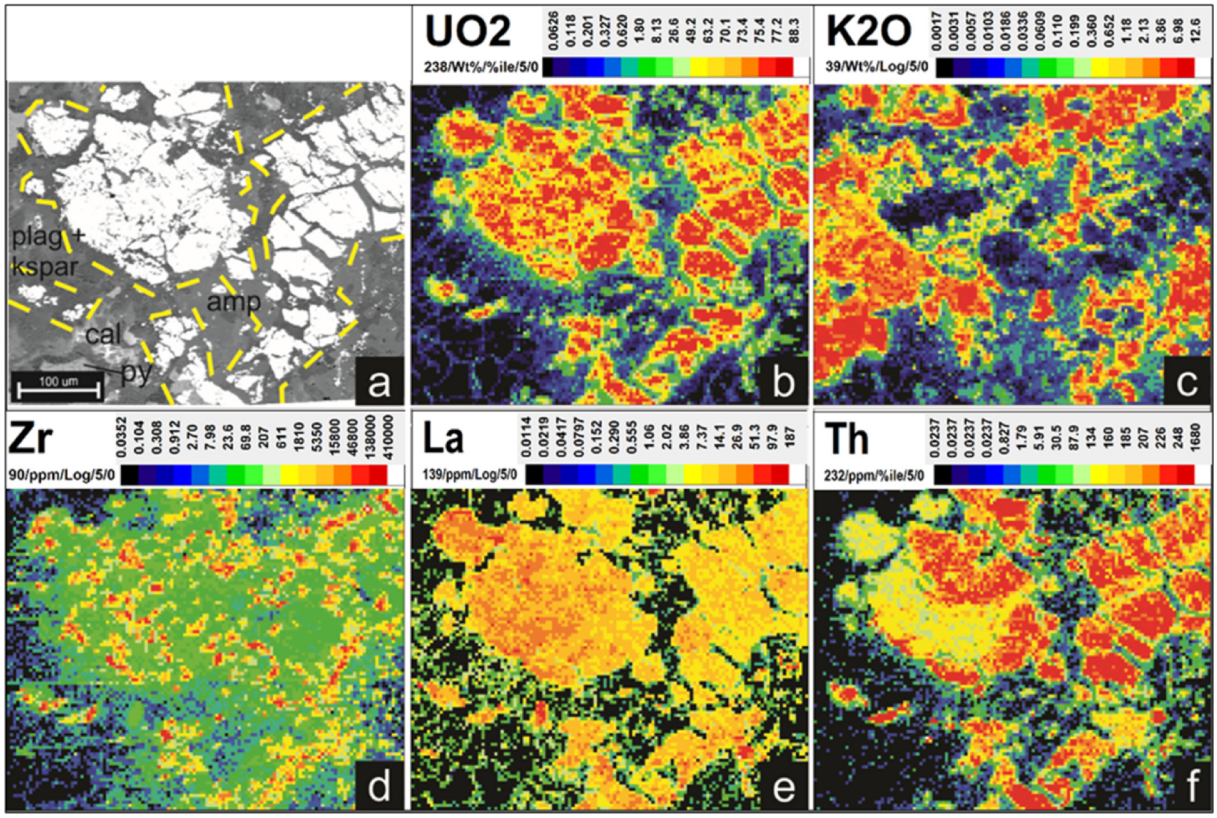


Fig. 8. LA-ICP-MS element maps of coarse-grained uraninite and pyrite in albite and amphibole from sample 18-CD-014b (Group 1) of the Kitts deposit.

the samples revealed the presence of an early and pervasive Na (albite), followed by Ca-Fe (ferro- and magnesio-hornblende, iron oxides) and then K-Fe alteration (K-feldspar, biotite, iron oxides) (Table 3) throughout the sample suite. These observations are consistent with the reported Na- and Ca-Fe- alteration overprint of the argillite at the Kitts deposit reported by Evans (1980). Although no temperature estimates were made on samples from the present study, fluid inclusions studies of IOCG systems indicate that high-temperature Na assemblages (albitites) form between 300° to 600 °C, Ca-Fe facies (amphibole-magnetite) at 400° to 800 °C, high-temperature K-Fe facies (K-feldspar ± biotite and magnetite) from 350° to 450 °C, and (4) low-temperature K-Fe facies (K-feldspar and hematite ± sericite ± carbonate ± chlorite) from 250° to 350 °C (Kish and Cuney, 1981; Bardina and Popov, 1992; Bastrakov et al., 2007; Chen et al., 2011; Harlov et al., 2002; Mark et al., 2006; Mark and Foster, 2000; Marschik et al., 2003; Monterio et al., 2008; Montreuil et al., 2016; Requia, 2003; Sidder et al., 1993; Somarin and Mumin, 2014; Xavier et al., 2010Sidor, 2000; Polito et al., 2009; Corriveau et al., 2016;).

The style of uranium mineralization, the host rocks and the distinctive alteration of the Kitts-Post Hill belt are similar to those reported from the Southern Breccia and Nori occurrences of the Great Bear magmatic zone (Montreuil et al., 2015; Potter et al., 2019), the albitite-hosted uranium deposits of Central Ukraine (Cuney et al., 2012), the Domes region uranium deposits of Zambia (Eglinger et al., 2013, 2014) and the Mistamisk albitite veins of Quebec (Kish and Cuney, 1981). Uranium mineralization of all these deposits is hosted in metasedimentary rocks (with the exception of some granitic-hosted deposits in Central Ukraine), which have experienced similar Na, Ca (+/−Mg, Fe) and K-Fe metasomatic alteration, similar metamorphic conditions and are controlled by analogous tectonic and deformational structures.

Uraninite mineralization from the Kitts-Post Hill belt and the Southern Breccia occurrences (Montreuil et al., 2015) is hosted by metasedimentary rocks and locally associated with pyrite-chalcopyrite-molybdenite that precipitated as a high-temperature K-Fe alteration facies (K-feldspar-biotite-magnetite). Accessory minerals such as allanite, galena, barite and scheelite observed in the Kitts-Post Hill belt (Fig. 4) are also present at the Southern Breccia (cf. Montreuil et al., 2015; Potter et al., 2019). In the Gear deposit, co-precipitation of uraninite with hedenbergite, magnesio- and ferro-hornblende, magnetite, andradite and talc is consistent with skarn-type alteration described in the Great Bear magmatic zone, which is commonly spatially associated with later than Na-alteration (Corriveau et al., 2016; Montreuil et al., 2016). Similar paragenetic relationships are described from the Central Ukraine albitite-hosted uranium deposits (Cuney et al., 2012).

The Nori occurrence of the Great Bear magmatic zone is hosted in meta-siltstones associated with stratabound to discordant, high-temperature K-Fe facies alteration assemblages (Gandhi, 1984; Ootes et al., 2010). Regionally, the Nori occurrence records Na-facies alteration (albite), high-temperature Ca-Fe facies alteration (amphibole, amphibole-magnetite and magnetite) and K-Fe facies alteration (+/−magnetite–K-feldspar breccia zones) (Corriveau et al., 2010, 2018). The mineral assemblages, fluid inclusion analyses and timing of mineralization led Corriveau et al. (2010, 2018) and Ootes et al. (2010) to suggest that the showings represent an early expression of an IOCG deposit within a regional IOAA system. Unlike uraninite mineralization observed in the Kitts-Post Hill belt, uraninite from the Nori occurrence is hosted in biotite-magnetite veins, and associated with tourmaline, K-feldspar, molybdenite, allanite, pyrite and chalcopyrite (Ootes et al., 2010). However, the host rocks and alteration styles are similar to that observed within the Kitts-Post Hill belt sample suite.

The Kitts-Post Hill belt mineralization is also similar to that of the Central Ukraine albitite deposits, which are characterized by Na- and Ca-Fe-, and K-Fe- alteration assemblages (Cuney et al., 2012). In these deposits, skarn-like andradite alteration is similar to that of the Gear deposit, and occurs in high temperature Ca-Fe alteration facies (Cuney et al., 2012). In the Central Ukraine, the K-Fe- alteration facies that hosts uranium mineralization comprises calcite, biotite, iron oxide and sulfides; and is somewhat similar to the uraninite-calcite-hematite vein-

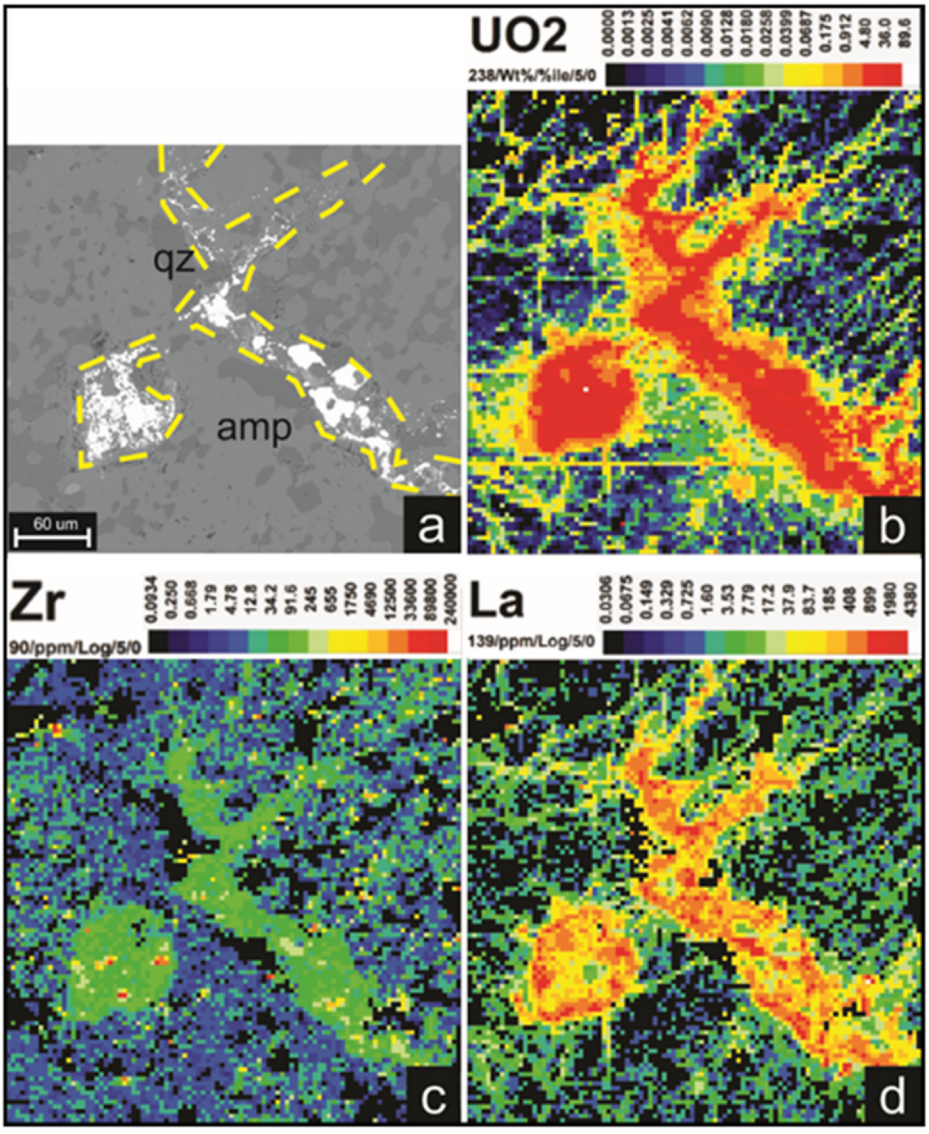


Fig. 9. LA-ICP-MS element maps of a fine-grained uraninite veinlet cutting amphibole and quartz from sample GS-08-267 (Group 3) of the Kitts deposit.

hosted assemblage observed in the Kitts-Post Hill belt (Evans, 1980; Sparkes, 2017).

The Domes region of the Pan-African Lufilian belt in Zambia is host to both copper and cobalt deposits, as well as syn-metamorphic uranium occurrences (Meneghel, 1981; Mercadier et al., 2011; Eglinger et al., 2013, 2014). The host rocks to the mineralization are dominantly carbonaceous quartzite and quartz-mica schist, and fluid inclusions in syn-metamorphic quartz veins suggest two uranium mineralization events (Meneghel, 1981; Eglinger et al., 2014). The uranium mineralization is associated with amphibolite facies metamorphism and Ca-Na metasomatism that broadly resembles features from the Kitts-Post Hill belt.

Kish and Cuney (1981) described the Mistamisk uranium deposit as uraninite-albite veins hosted in an argillite unit, where the wall-rock was pervasively Na-metasomatized and metamorphosed to greenschist facies. Furthermore, locally constrained weak to moderate K-alteration has been recognized in the Mistamisk boulder field (Desrochers, 2016). Widespread IOAA type alteration (Na, Ca-Fe, high- and low-temperature K-Fe facies) led Corriveau et al. (2014) to propose a possible genetic link between the Mistamisk deposit and a regional IOAA system. These suggested alteration facies were later confirmed by drilling and exploration work in the area (Desrochers, 2016). The Mistamisk deposit and Kitts-Post Hill belt have similar host rocks, local and regional alteration facies and regional metamorphic conditions.

Using limited whole rock geochemistry of the Kitts-Post Hill belt from the geochemical dataset of Acosta-Góngora et al. (2018), plotted on the IOCG discrimination plots of Montreuil et al. (2013), samples from the Kitts-Post Hill belt exhibit Na, Ca-Fe, K-Fe and K facies alteration typical of IOAA systems (Fig. 12b). The presence of these alteration facies is supported by combining the element molar proportion "bar codes" of key elements of the IOAA alteration assemblages (Corriveau et al., 2018) to illustrate the significant Na, Ca-Fe and in some cases, K-Fe and K alteration relative to type examples of unaltered rock (Fig. 12a). The presence of potential K and K-Fe alteration is particularly interesting, as this type of alteration has not been reported in the CMB and is the alteration facies associated with hematite and magnetite-group IOCG deposits (Corriveau et al., 2010, 2016).

In summary, the Kitts-Post Hill belt is characterized by multiple alteration assemblages that are typical of IOAA-type deposits (Na, Ca-Fe and K-Fe), where uraninite is hosted in Ca-Fe alteration, in spatial and syn-genetic association with K-Fe alteration (Corriveau et al., 2010, 2016).

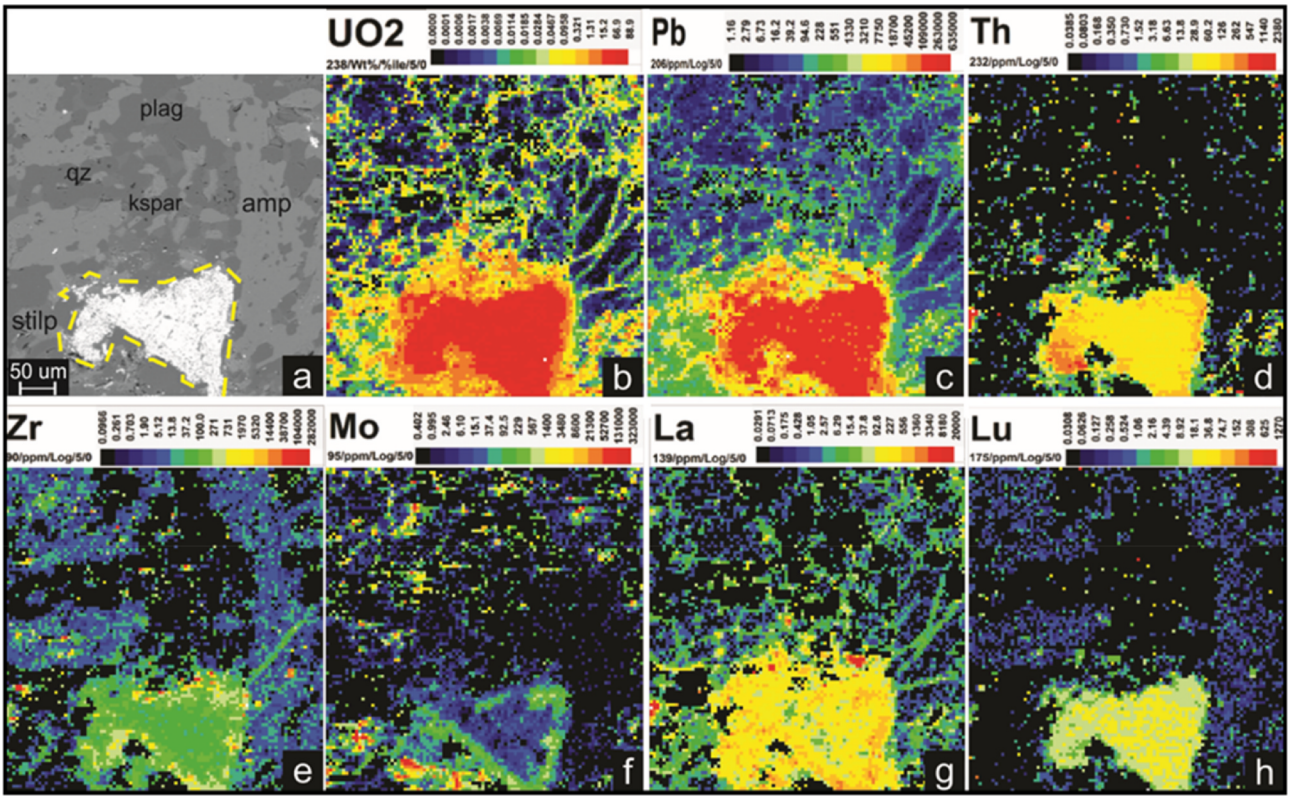


Fig. 10. LA-ICP-MS element maps of coarse-grained uraninite in albite, K-feldspar, amphibole and quartz from sample GS-08-267 (Group 3) of the Kitts deposit, highlighting the remobilization of U (b), Pb (c) and La (g) from uraninite along fractures.

6.2. Uraninite geochemistry

Based on chondrite-normalized REE patterns, three different populations of uraninite are recognized within the Kitts deposit. Based on U/Th ratios and total REE contents, the majority of samples from Kitts reflect low temperature (< 350 °C) hydrothermal conditions (Fig. 13) despite being hosted in mineral assemblages that form at higher temperatures–although a higher temperature (e.g., > 450 °C) signature is observed in group 3 samples (sample 17-CD-027; Fig. 13). These compositional differences and trace element maps indicating remobilization of certain elements from uraninite (Figs. 9–11) could reflect an early higher temperature event followed by subsequent alteration of uraninite by late lower temperature hydrothermal fluids.

The contrasting europium anomalies could be interpreted as a variation in oxygen fugacity between the primary and remobilizing fluids (Drake, 1975). As such, these anomalies could reflect fluids that have interacted with plagioclase-rich rocks, whereby the Ca^{2+} site in the plagioclase and Ca-Fe amphibole, which selectively concentrated europium during crystallization, releases europium when altered (Lottermoser, 1992). The positive europium anomaly therefore may be a result of uraninite having formed later than Na-facies alteration and Ca-Fe-facies alteration (amphibole), from fluids that had interacted with these minerals. Positive europium anomalies in chondrite-normalized REE patterns are rare in uraninite (Frimmel et al., 2014), but such features were observed in deposits of the Pan-African Lufilian belt (Eglinger et al., 2014), and were interpreted to reflect high oxygen fugacity of the mineralizing fluid. At least two generations of hematization have been described from the CMB, one of which is linked to uranium mineralization (Gower et al., 1982; Sparkes and Kerr, 2008; Sparkes et al., 2016), indicating that oxidized fluids influenced uranium endowment at some point during their history.

Uranium mineralization in the Kitts-Post Hill belt sample suite is always associated with potassium, often in the form of fine-grained K-feldspar and biotite but also accessory minerals such as stilpnomelane. In the Gear deposit, uranium mineralization is associated with magnetite, and possibly hematite. Based on petrography and trace element chemistry, Potter et al. (in press) propose that primary uranium precipitation in IOAA systems occurs during the reduced, high temperature K-Fe (magnetite) facies alteration as the fluid temperatures decrease and pH neutralizes. Subsequent dissolution-reprecipitation and alteration of primary uraninite can occur during the transition from magnetite to hematite-bearing K-Fe alteration, expanding the uranium potential in IOCG systems from magnetite-to hematite-bearing deposits. The transition from magnetite to hematite reflects an increase in the oxidation state of the fluid (Hemingway, 1990; Corriveau et al., 2016), supporting the interpretation that the positive europium anomalies in chondrite normalized REE patterns of Group 2 uraninite reflect remobilization by oxidized fluids.

Chondrite normalized REE patterns in uraninite are interpreted to reflect the mineralizing source fluid or deposit type of the uraninite (Mercadier et al., 2011; Frimmel et al., 2014). Uraninite LA-ICP-MS data from the Mistamisk deposit (Lach et al., 2013; this study) yielded chondrite normalized REE patterns with some similarities to uraninite from the Kitts-Post Hill belt (Fig. 7). In particular, both deposits exhibit a slightly convex or bell shaped pattern centred on Gd-Tb (Fig. 7), high U/Th ratios (Fig. 13) and similar total REE concentrations to Group 3 uraninite. The Mistamisk data (Lach et al., 2013; this study) also plot within the low-temperature hydrothermal field, close to and overlapping the Kitts data (Fig. 13). However, as shown by LREE disturbances during alteration of uraninite (Figs. 9–11), temperature estimates based solely on ΣREE (Fig. 13) may be less robust than estimates based on U/Th values. In summary, a roughly similar fluid source may be inferred based on uraninite geochemistry, host rocks, metamorphic conditions and alteration facies for the Kitts and the Mistamisk deposits.

Uranium oxides of the Central Ukraine albitite-hosted uranium

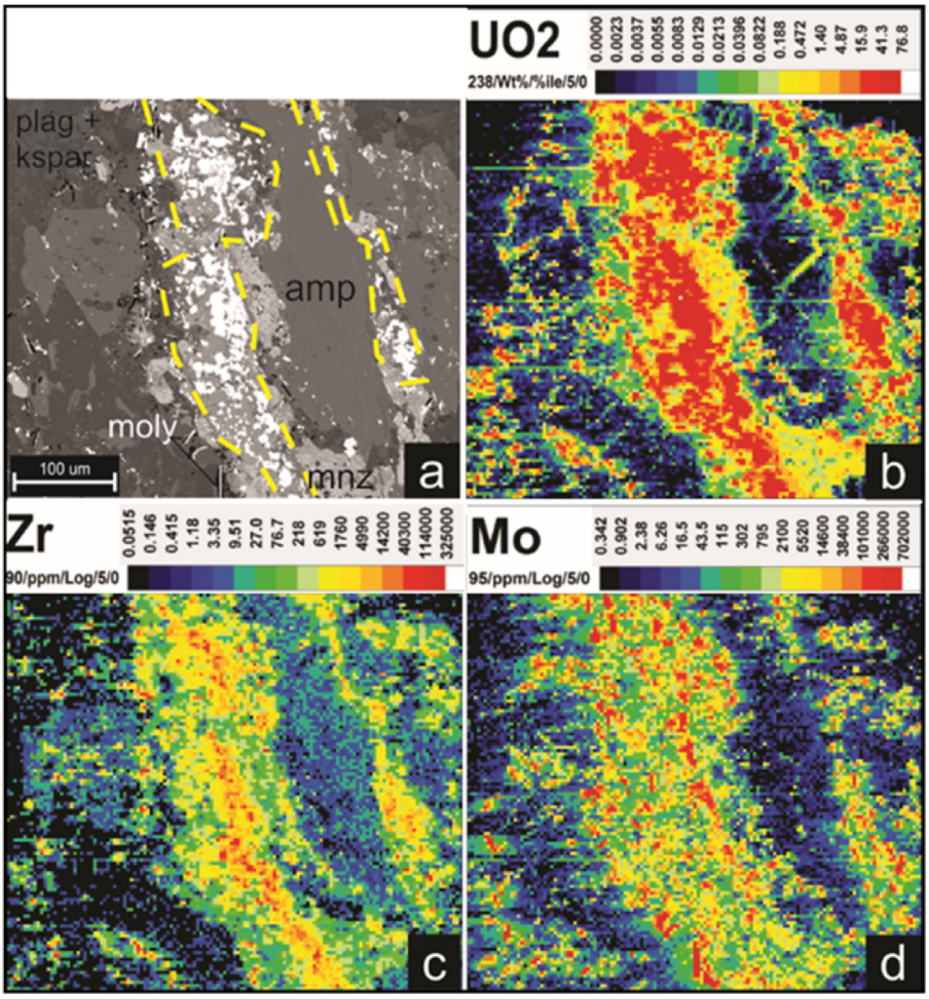


Fig. 11. LA-ICP-MS element maps of fine-grained uraninite-monazite-molybdenite veinlets cutting albite, amphibole and K-feldspar from sample 17-CD-27 (Group 3) of the Kitts deposit.

deposits and altered uraninite grains from the Nori uranium occurrence have low Th concentrations (8–2600 ppm Th; Cuney et al., 2012; Potter et al., in press). Uraninite from the Nori occurrence has similar chondrite normalized REE patterns to those of the Kitts deposit, in particular Group 3, which has the highest concentrations of REE (Fig. 7a, c). However, the elevated REE contents and chondrite-normalized patterns of the Nori prospect uraninite are indicative of formation by high temperate fluids, which is inconsistent with the temperature suggested by both the U/Th ratios and REE contents from the Kitts uraninite.

Eglinger et al. (2013) report chondrite normalized REE patterns for uraninite in the Domes region, which overlap with Group 3 of this study (Fig. 7c, e). The similar chondrite normalized REE patterns, combined with similarities in alteration styles and metamorphic conditions, point to a similar metasomatic-metamorphic fluid source for Group 3 uraninite and the Domes Region uraninite. The altered rims of Group 3 uraninites (Fig. 7e) are also similar to the patterns reported from the Kawanga deposit (Fig. 7f), a syn-metamorphic deposit within the Domes Region (Mercadier et al., 2011).

Martz et al. (2019) used variable REE contents in uraninite from unconformity-type uranium deposits to propose the presence of multiple generations of uraninite in such deposits. They propose that the LREE contents of uraninite increase significantly with alteration, whereas HREE contents slightly decrease. In our study, molybdenum was chosen to represent the threshold for classifying altered versus unaltered uraninite, as there is a clear Mo and La enrichment in the rim of sample GS-08-267 (Fig. 10). The LREE (La–Sm) are clearly enriched in the altered rim compared to the core, while the HREE (Gd–Lu) are similar for both the “altered” and “unaltered” REE patterns. This LREE enrichment in altered uraninite confirms the results of Martz et al. (2019), which show that LREE in particular, may be more easily mobilized from uraninite than previously thought (Fig. 7e).

The elevated zirconium contents in uraninite of the Kitts deposit resemble patterns described from uranium oxides within the albitite-hosted uraninite of Central Ukraine (Cuney et al., 2012) and the Southern Breccia corridor (Potter et al., 2019, in press). Cuney et al. (2012) and Montreuil et al (2016) propose high-temperature, alkaline fluids (i.e., elevated $Na+/K+$ and $Na+/H+$ ratios) during Ca-Fe metasomatism. Alkaline pH favours elevated uranium and zirconium solubilities as hydroxyl complexes (Romberger, 1984; Wood, 2005), whereas Ca, Mg and Fe are weakly mobile (Azimov and Bushmin, 2007). In the literature, zirconium mobility in hydrothermal fluids is commonly linked to formation of both fluoride and hydroxyfluoride species at high temperatures (Keppler and Wyllie, 1991; Salvi et al., 2000; Wood, 2005; Migdisov et al., 2009, 2011). However, the lack of F-bearing minerals in the samples supports the transport of uranium and zirconium as hydroxyl complexes in the Kitts-Post Hill belt.

Uraninite commonly show grain boundary enrichment or zoning in Zr, Th, Mo and LREE throughout the sample suite from the Kitts deposit (Fig. 10). This is possible evidence for incursion of acidic fluids after primary alteration and mineralization. Unlike LREE, HREE are not enriched in the groundmass, fractures or grain boundaries, and are therefore not affected by remobilization in the same way as the LREE

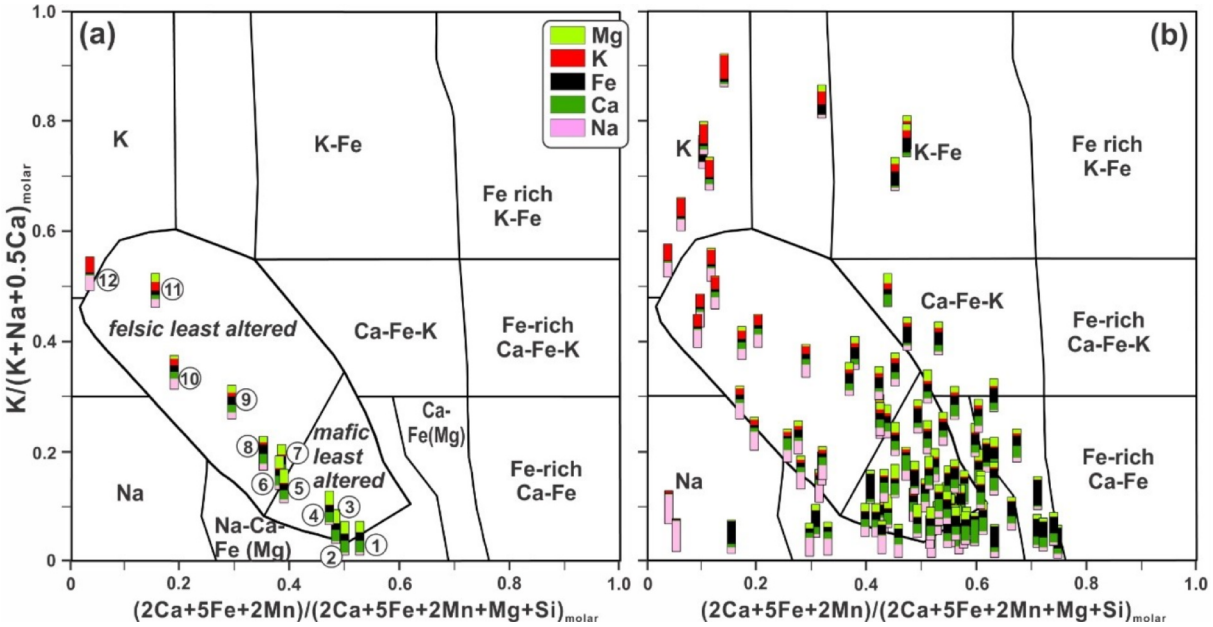


Fig 12. IOCG alteration discrimination plot of Montreuil et al. (2013) combined with the molar proportion "bar codes" of IOAA index cations (Na, Ca, Fe, K, Mg) of Corriveau et al. (2018) illustrating: (a) the composition of unaltered reference rock types selected from published data modified from Potter et al. (in press) and (b) samples of host rocks from in the Kitts-Post Hill trend. While a limited dataset, the samples from Kitts-Post Hill exhibit significant Na and Ca-Fe, and minor K-Fe alteration. Unaltered reference rock types in (a) from: 1 – Mid-oceanic ridge basalt (MORB), Keleman et al. (2014); 2 – N-MORB, Gale et al. (2003); 3 – oceanic basalt, 4 – continental crust, 5 – oceanic arc andesite, 6 – continental arc andesite, Keleman et al. (2014); 7 – bulk continental crust, Rudnick and Gao (2014); 8 – continental arc granite, 10 – calc alkaline granite, Kemp and Hawkesworth (2005); 9 – upper continental crust, Rudnick and Gao (2014); 11 – syn-collisional granite, 12 – volcanic arc granite, Pearce et al. (1984).

(Fig. 10g, h). Given the contrasting REE behaviour, fluids altering uraninite may have been Cl-rich, as LREE are more mobile in Cl-rich fluids (Migdisov et al., 2016).

In summary, the trace element signatures of uraninite from the Kitts deposit indicate a primary signature that is largely overprinted by a lower temperature hydrothermal signature (i.e. higher U/Th and lower REE concentrations). Three distinct REE chondrite normalized patterns are recognized in the Kitts uraninite, suggesting three different populations of uraninite. The uraninite is geochemically similar to material from other known metasomatic – metamorphic uranium deposits (notably Mistamisk and the Domes Region). Light REE, Zr, Mo and Th are enriched in altered rims of some uraninite grains relative to their cores, indicating significant alteration and or recrystallization by later fluids.

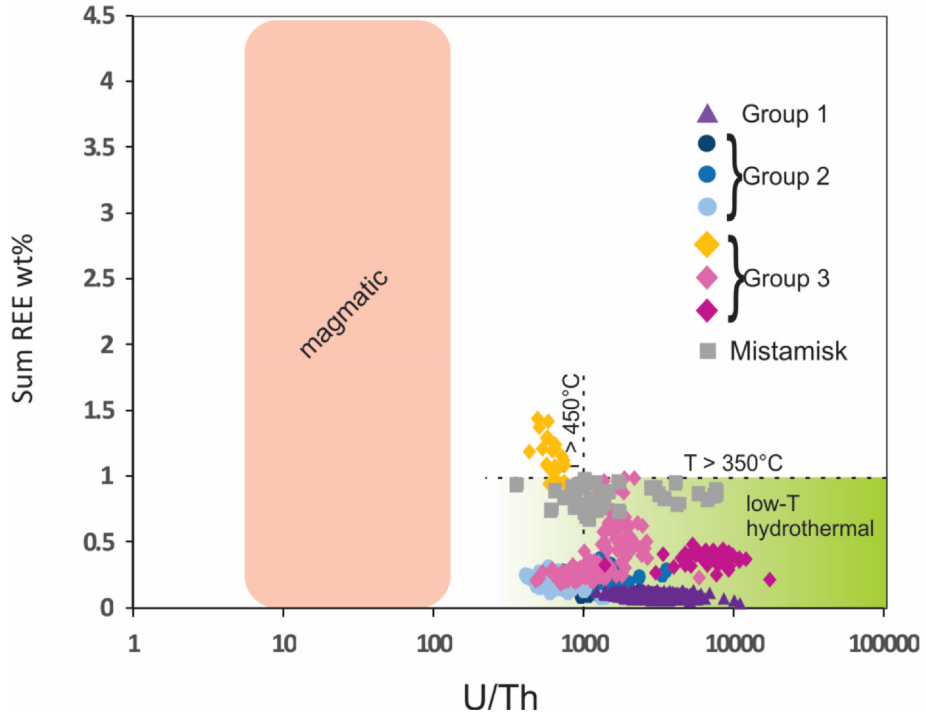


Fig. 13. Total REE content (wt%) versus U/Th of samples analyzed by LA-ICP-MS, modified from Frimmel et al. (2014).

6.3. Genetic links between mineralization and regional tectono-metamorphism

The three separate uraninite groups defined by EPMA data (Table 4) and chondrite-normalized uraninite patterns (Fig. 7) support the interpretation of at least two events that disturbed the primary uraninite mineralization within the Kitts deposit. The U/Th ratios and total REE contents of uraninite from the four samples suggest an order of mineralization from oldest to youngest consistent with Group 3 being oldest, and Group 1 being youngest, with Group 2 forming in an intermediate stage. Variations in U/Th determined by EPMA support a later uranium and lead mobility event that altered the U/Pb ratios of uraninite, possibly one of the many metamorphic and/or plutonic events in the CMB. Support for this process is observed in Figure 10c, which shows lead enrichment along fractures and in the altered uraninite rim. Thorium was less mobile during these events, (Fig. 10d), as lead is more easily leached from uraninite and mobile than thorium in typical geological fluids (Alexandre and Kyser, 2005).

Element remobilization in the Kitts-Post Hill belt is suggested by the uraninite geochemistry and confirmed by the LA-ICP-MS maps, supporting suggestions by previous studies of the Central Mineral Belt (Sparkes and Kerr, 2008; Tracey, 2009; Sparkes et al., 2010). Mineralization in the Kitts-Post Hill belt has not been directly dated, but Sparkes et al. (2010) interpret the Kitts primary uranium mineralization as older than 1882 Ma but younger than 2018 Ma based on dates from pre-mineralization host rocks and a younger, cross-cutting dyke. All EPMA U-Pb ages (excluding the outliers) reported in Duffett (2019) are younger than the mineralization age bracket defined by Sparkes et al. (2010), but radiogenic lead loss in uraninite older than 1000 Ma causes uncertainty in EPMA ages (Bowles, 2015) and lead loss has been documented in uraninite samples from the Kitts deposit (Davis, 2002).

The regional-scale tectono-metamorphic events experienced in the area represent potential driving forces for fluid flow, heat production and element remobilization in the area, which are key ingredients in the development of IOAA type deposits but also subsequent remobilization of metals (Corriveau et al., 2010; Montreuil et al., 2016). The ca. 1802 Ma Long Island pluton (Kerr et al., 1992) could represent a potential source of heat for the element remobilization in the Kitts-Post Hill belt, due to its geographic proximity. Younger titanite ages of 1794 ± 2 Ma, 1761 ± 2 Ma and 1746 ± 2 Ma from intrusive rocks in the Kaipokok Bay area (Kerr et al., 1992) suggest that the area was thermally and tectonically active for up to 50 Ma after emplacement of the Long Island pluton, providing further support for our interpretation of multiple uranium remobilization events in the area.

7. Conclusion

The alteration and mineral assemblages presented in this study suggest that uranium mineralization in the Kitts-Post Hill belt of the CMB is best classified as metasomatic uranium, with a potential IOAA linkages characterized by regional Na, Ca-Fe and K-Fe alteration. More specifically, the Kitts mineralization is geochemically similar to both the Mistamisk deposit, an albitite-hosted vein uranium deposit with potential IOAA linkages (Corriveau et al., 2014), and the Domes region deposits of Zambia, where the U mineralizing fluid is interpreted to have a Ca-Na metasomatic origin (Eglinger et al., 2014).

Differences in uraninite geochemistry point to a complex hydrothermal fluid history, where the primary signatures may have been altered by multiple regional metamorphic-plutonic episodes, resulting in at least three populations of uraninite at Kitts. The zirconium enrichment associated with uraninite and mineral assemblages suggests high temperature primary alkaline fluids that were capable of moving HFSE. Enrichment of Zr, LREE, U and Pb along grain boundaries and fractures within the matrix support late remobilization of these elements during alteration of the uraninite. The enrichment of LREE in rims compared to the cores of uraninite grains support the findings of Martz et al. (2019) suggesting that disruption of primary REE signatures is possible under certain fluid conditions. The greater stability and higher solubility of LREE-chloride species relative to HREE-chloride species (Migdisov et al., 2016) supports alteration and preferential mobility of LREE relative to HREE by Cl-rich fluids at the Kitts deposit. These results also indicate that temperature estimates based on total REE and thorium contents may be disturbed by alteration processes.

The chondrite-normalized REE patterns, total REE contents and U/Th ratios of uraninite at the Kitts deposit collectively suggest a metasomatic fluid source for the Kitts-Post Hill belt deposits similar to that of the Domes region in Africa and the Mistamisk deposit in Québec. Uraninites from the Kitts deposit exhibit LREE/HREE ratios that increase with increasing alteration and remobilization. The positive europium anomalies of Group 2 uraninite may reflect remobilization by fluids with higher oxygen fugacity (Drake, 1975), which is independently supported by the late hematite alteration documented in the region (Hemingway, 1990).

Declaration of Competing Interest

The authors declare that they have no known competing financial interests or personal relationships that could have appeared to influence the work reported in this paper.

Acknowledgements

This paper is a contribution to the metasomatic uranium activity of the Targeted Geosciences Initiative (TGI) program. Additional support was received by CLD in the form of scholarships and bursaries from the Research Affiliate Program of the Government of Canada, Carleton University and Nunatukavut of Labrador. We are thankful for the collaboration with the Newfoundland and Labrador Geological Survey, specifically Greg Sparkes and Glenn Penney. We thank Pat Hunt and Chris Koblynski of the Geological Survey of Canada for their expertise in SEM techniques. We thank Glenn Poirier of the University of Ottawa and Katherine Venance of the Geological Survey of Canada for their EPMA expertise. We thank Andy Kerr and the anonymous reviewer for their peer-reviews. This paper is a component of a M.Sc. thesis by CLD under the supervision of EGP and BLC.

Appendix A. Supplementary data

Supplementary data to this article can be found online at https://doi.org/10.1016/j.oregeorev.2020.103720.

References

Xavier, R, Monteiro, L, de Souza Filho, C, Torresi, I, 2010. The iron oxide copper-gold deposits of the Carajas Mineral Province, Brazil: an updated and critical review. Hydrothermal Iron Oxide Copper-Gold and Related Deposits: A Global Perspective-Advances in the Understanding of IOCG Deposits 3.

Acosta-Góngora, P., Potter, E.G., Corriveau, L., Lawley, C.J.M., Sparkes, G.W., 2018. Geochemistry of U ± Cu ± Mo ± V mineralization, Central Mineral Belt, Labrador: differentiating between mineralization styles using a principal component analysis approach. In: Rogers, N. (Ed.), Targeted Geoscience Initiative: 2018 Report of Activities. Geological Survey of Canada, Open File 8549, pp. 381–391.

Alexandre, P., Kyser, T.K., 2005. Effects of cationic substitution and alteration in uraninite and implications for the dating of uranium deposits. Can. Mineral. 43, 1005–1017.

Azimov, P.Y., Bushmin, S.A., 2007. Solubility of minerals and metasomatic rocks in hydrothermal solutions of varying acidity: thermodynamic modeling at 400–800 °C and 1–5 kbar. Geochem. Int. 45, 1210–1234.

BHP, 2018. BHP Billiton Limited annual report 2018, 300 p. Available from: < www.bhp.com/investor-centre > .

Bardina, N, Popov, V, 1992. CLASSIFICATION OF METASOMATIC ROCKS AND FACIES OF SHALLOW METASOMATISM. International Geology Review 34 (2), 187–196 In this issue.

Bastrakov, E, Skirrow, R, Davidson, G, 2007. Fluid Evolution and Origins of Iron Oxide Cu-Au Prospects in the Olympic Dam District, Gawler Craton, South Australia. Economic Geology 102 (8), 1415–1440.

Bowles, J., 2015. Age dating from electron microprobe analyses of U, Th, Ph: geological

advantages and analytical difficulties. Microsc. Microanal. 21, 1114–1122.
Bruneton, P., Cuney, M., Dahlkamp, F., Zaluski, G., 2014. IAEA geological classification of uranium deposits. In: Proceedings of the International Symposium on Uranium Raw Material for the Nuclear Fuel Cycle (URAM 2014), Vienna, pp. 8–18.
Cadman, A.C., Heaman, L., Tarney, J., Wardle, R., Krogh, T.E., 1993. U-Pb geochronology and geochemical variation within two Proterozoic mafie dyke swarms, Labrador. Can. J. Earth Sci. 30, 1490–1504.
Corriveau, L., Williams, P., Mumin, A.H., 2010. Alteration vectors to IOCG mineralization from uncharted terranes to deposits. In: Corriveau, L., Mumin, A.H., (Eds.), Exploring for Iron Oxide Copper-gold Deposits: Canada and Global Analogues. Geological Association of Canada, Short Course Notes 20, pp. 89–110.
Corriveau, L., Nadeau, O., Montreuil, J.-F., Desrochers, J.-P., 2014. Report of activities for the Core Zone: Strategic geomapping and geoscience to assess the mineral potential of the Labrador Trough for multiple metals IOCG and affiliated deposits, Canada. Geological Survey of Canada, Open File 7714, pp. 12, https://doi.org/10.4095/295529.
Corriveau, L., Potter, E.G., Montreuil, J.-F., Blein, O., Ehrig, K., and De Toni, A., 2018. Iron-oxide and alkali-calcic alteration ore systems and their polymetallic IOA, IOCG, skarn, albitite-hosted U ± Au ± Co, and affiliated deposits: a short course series. Part 2: overview of deposit types, distribution, ages, settings, alteration facies, and ore deposit models. In: Geological Survey of Canada, Scientific Presentation 81, 154 p.
Corriveau, L., Montreuil, J.-F., Potter, E.G., Ehrig, K., Mumin, A.H., Williams, P.J., in press. Alteration facies in IOCG and affiliated deposits: part 1 – Geology. In Corriveau, L., Potter, E.G., Mumin, A.H. (Eds.), Iron Oxide-Copper-Gold and Affiliated Deposits. Geological Association of Canada Special Paper 52.
Chen, H.Y., Clark, A.H., Kyser, T.K., 2011. Contrasted hydrothermal fluids in the Marcona-Mina Justa iron-oxide Cu (-Au-Ag) deposits, south-central Peru. Mineralium Deposita 46, 677–706.
Corriveau, Louise, 2007. **Iron oxide copper-gold deposits: a Canadian perspective**. **Mineral deposits of Canada: a synthesis of major deposit-types, district metallogeny, the evolution of geological provinces, and exploration methods**. Geological Association of Canada, pp. 307–328 In this issue.
Corriveau, L., Montreuil, J.-F., Potter, E.G., 2016. Alteration facies linkages among iron oxide copper-gold, iron oxide-apatite, and affiliated deposits in the Great Bear Magmatic Zone, Northwest Territories, Canada. Econ. Geol. 111, 2045–2072. https://doi.org/10.2113/econgeo.111.8.2045.
Culshaw, N., Ketchum, J., Barr, S., 2000. Structural evolution of the Makkovik Province, Labrador, Canada' Tectonic processes during 200 Myr at a Paleoproterozoic active margin. Tectonics 19, 961–977.
Culshaw, Nicholas, Peter, Reynolds, Sinclair, Gavin, Barr, Sandra, 2002. Amphibole and mica $^{40}Ar/^{39}Ar$ ages from the Kaipokok and Aillik domains, Makkovik Province, Labrador: towards a characterization of back-arc processes in the Paleoproterozoic. Canadian Journal of Earth Sciences 39, 749–764 In this issue.
Cuney, M., 2009. The extreme diversity of uranium deposits. Miner. Deposita 44, 3–9. https://doi.org/10.1007/s00126-008-0223-1.
Cuney, M, 2010. Evolution of Uranium Fractionation Processes through Time: Driving the Secular Variation of Uranium Deposit Types. Economic Geology 105 (3), 553–569 In this issue.
Cuney, M., Emetz, A., Mercadier, J., Mykchaylov, V., Shunko, V., Yuslenko, A., 2012. Uranium deposits associated with Na-metasomatism from central Ukraine: a review of some of the major deposits and genetic constraints. Ore Geol. Rev. 44, 82–106. https://doi.org/10.1016/j.oregeorev.2011.09.007.
Davis, W.J., 2002. Adventures in uraninite geochronology. In: Kositcin, N, Bodorkos, S (Eds.), **6th International SHRIMP Workshop – Program and Abstracts**. Geoscience Australia, pp. 38–40.
Desrochers, J.P., 2016. Exploration Report (fall 2014 drill Program) on the Sagar Property, Romanet Horst, Labrador Trough, Québec, Canada. Energizer Resources Inc, pp. 73.
Drake, M.J., 1975. The oxidation state of europium as an indicator of oxygen fugacity. Geochim. Cosmochim. Acta 39, 55–64. https://doi.org/10.1016/0016-7037(75)90184-2.
Duffett, C.L., 2019. The evolution of metasomatic uranium ore systems in the Central Mineral Belt of Labrador. MSc Thesis. Carleton University, Ottawa, ON, pp. 147.
Eglinger, A., André-Mayer, A.-S., Vanderhaeghe, O., Mercadier, J., Cuney, M., Decrée, S., Feybesse, J.-L., Milesi, J.-P., 2013. Geochemical signatures of uranium oxides in the Lufilian belt: from unconformity-related to syn-metamorphic uranium deposits during the Pan-African orogenic cycle. Ore Geol. Rev. 54, 197–213. https://doi.org/10.1016/j.oregeorev.2013.04.003.
Eglinger, A., Tarantola, A., Durand, C., Ferraina, C., Vanderhaeghe, O., André-Mayer, A.-S., Paquette, J.-L., Deloule, E., 2014. Uranium mobilization by fluids associated with Ca–Na metasomatism: a P – T – t record of fluid–rock interactions during Pan-African metamorphism (Western Zambian Copperbelt). Chem. Geol. 386, 218–237. https://doi.org/10.1016/j.chemgeo.2014.07.028.
Evans, D., 1980. Geology and petrochemistry of the Kitts and Michelin uranium deposits and related prospects, Central Mineral Belt, Labrador. Unpublished Ph.D. thesis. Queen's University, Kingston, Ontario, Canada, pp. 311.
Fabris, A., in press. Geochemical characteristics of IOCG systems: examples from the Olympic Cu-Au Province, South Australia. In: Corriveau, L., Potter, E.G., Mumin, A.H., (Eds.), Iron Oxide-Copper-Gold (IOCG) and Affiliated Deposits. Geological Association of Canada, Special Paper 52.
Fayek, M, Kyser, T, 1997. Characterization of multiple fluid-flow events and rare-earth-element mobility associated with formation of unconformity-type uranium deposits in the Athabasca Basin, Saskatchewan. Canadian Journal of Earth Sciences 35 (3), 627–658 In this issue.
Frimmel, H.E., Schedel, S., Brätz, H., 2014. Uraninite chemistry as forensic tool for provenance analysis. Appl. Geochem. 48, 104–121.
Fryer, Brian, Taylor, Richard, 1987. Rare-earth element distributions in uraninites: Implications for ore genesis. Chemical Geology 63 (1–2), 101–108 In this issue.
Gale, A., Dalton, C.A., Langmuir, C.H., Su, Y., Schilling, J.-G., 2003. The mean composition of ocean ridge basalts. Geochem. Geophys. Geosyst. 14, 489–518.
Gandhi, S., 1978. Geological setting and genetic aspects of uranium occurrences in the Kaipokok Bay-Big River area. Labrador. Econ. Geol. 73, 1492–1522.
Gandhi, S., 1984, Uranium in early Proterozoic Aillik Group, Labrador. In: Proterozoic Unconformity and Stratabound Uranium Deposits. J. Ferguson, (Ed.), IAEA, Vienna, Technical Doc. vol. 315, pp. 35–68.
Golder, H.Q., 1977. Feasibility study volume 2-geology and reserves and volume 6 geotechnical surveys for Kitts-Michelin project, Labrador, Newfoundland and Labrador Geological Survey, Assessment File LAB/0259, pp. 583.
Gower C.F. and Ryan, B., 1987, Two stage felsic volcanism in the Lower Proterozoic upper Aillik Group, Labrador, Canada: its relationship to syn- and postkinematic Plutonism: Geochemistry and Mineralization of Proterozoic Volcanic Suites. In: Pharaoh, T. C., Beckinsale, R. D., Rickard, D., (Ed.), Geological Society Special Publication vol. 33, pp. 201–210.
Gower C.F., Flanagan, M.J., Kerr, A., Bailet, D.G., 1982. Geology of the Kaipokok Bay – Big River area, Central Mineral Belt, Labrador. In: Newfoundland and Labrador Department of Mines and Energy, Mineral Development Division, Report, pp. 82–87.
Gower, Charles, Ryan, Bruce, 1986. Proterozoic evolution of the Grenville Province and adjacent Makkovik Province in eastern Labrador. Geological Association of Canada In this issue.
Gower, C.F., Schärer, U., Heaman, L.M., 1992. The Labradorian orogeny in the Grenville Province, eastern Labrador, Canada. Can. J. Earth Sci. 29, 1944–1957. https://doi.org/10.1139/e92-152.
Harlov, D.E., Förster, H-J., Nijland, T.G., 2002. Fluid-induced nucleation of REE-phosphate minerals in apatite: nature and experiment. Part I. Chlorapatite. American Mineralogist 87 (2–3), 245–261.
Hemingway, B.S., 1990. Thermodynamic properties for bunsenite, NiO, magnetite, Fe3O4, and hematite, Fe2O3 with comments on selected oxygen buffer reactions. Am. Mineral. 75, 781–790.
Hinchey, A., 2007. The Paleoproterozoic metavolcanic, metasedimentary and igneous rocks of the Aillik domain, Makkovik province, Labrador (NTS map area 13O/03). Current Research, Newfoundland and Labrador Department of Natural Resources Geological Survey, Report 07-1, pp. 25–44.
Hidaka, H, Gauthier-Lafaye, F, 2001. Neutron capture effects on Sm and Gd isotopes in uraninites. Geochimica et Cosmochimica Acta 65 (6), 941–949 In this issue.
Hidaka, H, Holliger, P, Shimuzu, H, Masuda, A, 1992. Lanthanide tetrad effect observed in the Oklo and ordinary uraninites and its implication for their forming processes. Geochemical Journal 337–346.
Hitzman, M.W., Oreskes, N., Einaudi, M.T., 1992. Geological characteristics and tectonic setting of proterozoic iron oxide (Cu-U-Au-REE) deposits. Precambr. Res. 58, 241–287. https://doi.org/10.1016/0301-9268(92)90121-4.
Hitzman, M.W., Valenta, R.K., 2005. Uranium in iron oxide-copper-gold (IOCG) systems. Econ. Geol. 100, 1657–1661. https://doi.org/10.2113/gsecongeo.100.8.1657.
Jackson, S.E., 2008a. Calibration strategies for elemental analysis by LA-ICP-MS. In: Sylvester, P. (Ed.), Laser Ablation-ICP-Mass Spectrometry in the Earth Sciences: Current Practices and Outstanding Issues. Mineralogical Association of Canada, Short Course Series, vol. 40, pp. 169–188.
Jackson, S.E., 2008b. LAMTRACE data reduction software for LA-ICP-MS. In: Sylvester, P. (Ed.), Laser Ablation-ICP-Mass Spectrometry in the Earth Sciences: Current Practices and Outstanding Issues. Mineralogical Association of Canada, Short Course Series, vol. 40, pp. 305–307.
Jochum, K.P., Willbold, M., Raczek, I., Stoll, B., Herwig, K., 2005. Chemical characterisation of the USGS reference glasses GSA-1G, GSC-1G, GSD-1G, GSE-1G, BCR-2G, BHVO-2G and BIR-1G using EPMA, ID-TIMS, ID-ICP-MS and LA-ICP-MS. Geostand. Geoanal. Res. 29, 285–302.
Keleman, P.B., Hanghøj, K., Greene, A.R., 2014. One view of the geochemistry of subduction-related magmatic arcs, with an emphasis on primitive andesite and lower crust. In: Rudnick, R.L., Holland, H.D., Turekian, K.K. (Eds.), Treatise on Geochemistry, second ed. Elsevier, Amsterdam, pp. 749–806.
Kemp, A.J., Hawkesworth, C.J., 2005. Granitic perspectives on the generation and secular evolution of the continental crust. In: Rudnick, R.L., Holland, H.D., Turekian, K.K. (Eds.), Treatise on Geochemistry, The Crust. Elsevier, Amsterdam, pp. 349–410.
Keppler, H., Wyllie, P.J., 1991. Partitioning of Cu, Sn, Mo, W, U, and Th between melt and aqueous fluid in the systems haplogranite–H2O–HCl and haplogranite–H2O–HF. Contrib. Miner. Petrol. 109, 139–150.
Kerr, A., Ryan, B., Gower, C., Wardle, R., 1996. The Makkovik province: extensions of the Ketilidian Mobile Belt in mainland North America. In: Brewer, T. (Ed.), Precambrian crustal evolution in the North Atlantic region. Geological Society Special Publication, vol. 112, pp. 155–177.
Kerr, A., Krogh, T.E., Corfu, E., Scharer, U., Gandhi, S.S., Kwok, Y.Y., 1992. Episodic Early Proterozoic granitoid plutonism in the Makkovik Province, Labrador: U-Pb geochronological data and geological implications. Can. J. Earth Sci. 29, 1166–1179.
Ketchum, J.W.F., Barr, S.M., Culshaw, N.G., White, C.E., 2001. U-Pb ages of granitoid rocks in the northwestern Makkovik Province, Labrador: evidence for 175 million years of episodic synorogenic and postorogenic plutonism. Can. J. Earth Sci. 38, 359–372. https://doi.org/10.1139/cjes-38-3-359.
Ketchum, J.W., Culshaw, N.G., Dunning, G.R., 1997. U-Pb geochronologic constraints on Paleoproterozoic orogenesis in the northwestern Makkovik Province, Labrador, Canada. Can. J. Earth Sci. 34, 1072–1088.
Ketchum, J., Culshaw, N.G., Barr, S.M., 2002. Anatomy and orogenic history of a Paleoproterozoic accretionary belt: the Makkovik Province, Labrador, Canada. Can. J. Earth Sci. 34, 1072–1088.
Kish, L., Cuney, M., 1981. Uraninite-albite veins from the Mistamisk Valley of the

Labrador Trough, Quebec. Mineral. Mag. 44, 471–483.
Kontonikas-Charos, A., Ciobanu, C.L., Cook, N., 2014. Albitization and redistribution of REE and Y in IOCG systems: insights from Moonta-Wallaroo, Yorke Peninsula, South Australia. Lithos 208–209, 178–201.
Lach, P., Mercadier, J., Dubessy, J., Boiron, M.-C., Cuney, M., 2013. In situ quantitative measurement of rare earth elements in uranium oxides by laser ablation-inductively coupled plasma-mass spectrometry. Geostand. Geoanal. Res. 37, 277–296.
Lawley, C.J.M., Creaser, R.A., Jackson, S.E., Yang, Z., Davis, B.J., Pehrsson, S.J., Dubé, B., Mercier-Langevin, P., Vaillancourt, D., 2015. Unraveling the Western Churchill Province Paleoproterozoic Gold Metallotect: constraints from Re-Os Arsenopyrite and U-Pb Xenotime geochronology and LA-ICP-MS arsenopyrite trace element chemistry at the BIF-hosted meliadine Gold District, Nunavut, Canada. Econ. Geol. 110, 1425–1454. https://doi.org/10.2113/econgeo.110.6.1425.
Lawley, C.J.M., Petts, D.C., Jackson, S.E., Zagorevski, A., Pearson, D.G., Kjarsgaard, B.A., Savard, D., Tschirhart, V., 2020. Precious metal mobility during serpentinization and breakdown of base metal sulphide. Lithos 354–355, 105278.
Locock, A.J., 2014. An Excel spreadsheet to classify chemical analyses of amphiboles following the IMA2012 recommendations. Comput. Geosci. 62, 1–11.
Lottermoser, B.G., 1992. Rare earth elements and hydrothermal ore formation processes. Ore Geol. Rev. 7, 25–41. https://doi.org/10.1016/0169-1368(92)90017-F.
Maas, R, McCulloch, M, 1990. A search for fossil nuclear reactors in the Alligator River Uranium Field, Australia: Constraints from Sm, Gd and Nd isotopic studies. Chemical Geology 88 (3–4), 301–315 In this issue.
Mark, G, Foster, D.R.W., 2000. Magmatic albite-actinolite-apatite-rich rocks from the Cloncurry district, Northwest Queensland, Australia. Lithos 223–245 In this issue.
Mark, G, Oliver, N.H.S., Williams, P.J., 2006. Mineralogical and chemical evolution of the Ernest Henry Fe oxide-Cu-Au ore system, Cloncurry district, northwest Queensland, Australia. Mineralium Deposita 40, 769–801 In this issue.
Marschik, R, Massimo, C, Fontboté, L, 2003. Implications of Pb isotope signatures of rocks and iron oxide Cu-Au ores in the Candelaria-Punta del Cobre district, Chile. Mineralium Deposita 38, 900–912.
Marten, B., 1977. The relationship between the Aillik Group and the Hopedale gneiss, Kaipokok Bay, Labrador. Unpublished PhD thesis. Memorial University of Newfoundland, Canada, pp. 249.
Martz, P., Mercadier, J., Perret, J., Villeneuve, J., Deloule, E., Cathelineau, M., Quirt, D., Doney, A., Ledru, P., 2019. Post-crystallization alteration of natural uraninites: implications for dating, tracing, and nuclear forensics. Geochim. Cosmochim. Acta 249, 138–159. https://doi.org/10.1016/j.gca.2019.01.025.
McDonough, W., Sun, S., 1995. The composition of the Earth. Chem. Geol. 120, 223–253.
Meneghel, L., 1981. The occurrence of uranium in the Katanga System of northwestern Zambia. Econ. Geol. 76, 56–68. https://doi.org/10.2113/gsecongeo.76.1.56.
Mercadier, J., Cuney, M., Lach, P., Boiron, M.-C., Bonhoure, J., Richard, A., Leisen, M., Kister, P., 2011. Origin of uranium deposits revealed by their rare earth element signature: origin of U deposits revealed by the rare earth elements. Terra Nova 23, 264–269. https://doi.org/10.1111/j.1365-3121.2011.01008.x.
Migdisov, A.A., Williams-Jones, A.E., Wagner, T., 2009. An experimental study of the solubility and speciation of the Rare Earth Elements (III) in fluoride- and chloride-bearing aqueous solutions at temperatures up to 300 °C. Geochim. Cosmochim. Acta 73, 7087–7109.
Migdisov, A.A., Williams-Jones, A.E., van Hinsberg, V., Salvi, S., 2011. An experimental study of the solubility of baddeleyite (ZrO2) in fluoride-bearing solutions at elevated temperature. Geochim. Cosmochim. Acta 75, 7426–7434.
Migdisov, A., Williams-Jones, A., Brugger, J., Caporuscio, F., 2016. Hydrothermal transport, deposition, and fractionation of the REE: experimental data and thermodynamic calculations. Chem. Geol. 439, 13–42. https://doi.org/10.1016/j.chemgeo.2016.06.005.
Monterio, L, Xavier, R, Hitzman, M, Juliani, C, de Souza Filho, C, de R. Carvalho, E, 2008. Mineral chemistry of ore and hydrothermal alteration at the Sossego iron oxide–-copper–gold deposit, Carajás Mineral Province, Brazil. Ore Geology Reviews 34, 317–336.
Montreuil, J.-F., Corriveau, L., Grunsky, E.C., 2013. Compositional data analysis of hydrothermal alteration in IOCG systems, Great Bear magmatic zone, Canada, To each alteration type its own geochemical signature. Geochem. Explor., Environ. Anal. 13, 229–247.
Montreuil, J., Corriveau, L., Potter, E.G., 2015. Formation of albitite-hosted uranium within IOCG systems: the Southern Breccia, Great Bear magmatic zone, Northwest Territories, Canada. Miner. Deposita 50, 293–325. https://doi.org/10.1007/s00126-014-0530-7.
Montreuil, J.F., Potter, E.G., Corriveau, L.C., Davis, W.J., 2016. Element mobility patterns in magnetite-group IOCG systems: The Fab IOCG system, Northwest Territories, Canada. Ore Geology Reviews 72, 562–584.
Montreuil, J., Potter, E.G., De Toni, A., 2016. On the relationship between alteration facies and metal endowment of iron oxide-alkali-altered systems, Southern Great Bear magmatic zone. Canada. Econ. Geol. 111, 2139–2168.
Nunn G., A. G., Thomas, A., Kroght, E., 1985. The Labradorian orogeny: geochronological database. In: Current research for 1984, Newfoundland Department of Mines and Energy, Mineral Development Division, Report 85-1, pp. 43–54.
OECD, 2018. Uranium 2018: Resources, Production and Demand. Organisation for Economic Co-operation and Development, Nuclear Energy Agency, no 7413, pp. 462.
Ootes, L., Goff, S., Jackson, V.A., Gleeson, S.A., Creaser, R.A., Samson, I.M., Evensen, N., Corriveau, L., Mumin, A.H., 2010. Timing and thermochemical constraints on multi-element mineralisation at the Nori/RA Cu–Mo–U prospect, Great Bear magmatic zone, Northwest Territories, Canada. Miner. Deposita 45, 549–566. https://doi.org/10.1007/s00126-010-0291-x.
Paladin Energy Ltd. 2019. Michelin project, Labrador Canada. Project brochure dated September 2019. Available at: < www.paladinenergy.com.au/project/michelin-canada > .
Paradis, S., Jackson, S.E., Petts, D., Simandl, G.J., D'Souza, R.J., 2020. Distribution of trace elements in pyrite of carbonate-hosted sulphide deposits of southern British Columbia, Canada: in TGI-5 Base Metals synthesis volume.
Pagel, M, Pinte, G, Rotach-Toulhoat, N, 1987. The Rare Earth Elements in Natural Uranium Oxides. B. Mineralogical and Geochemical Studies In press.
Pearce, J.A., Harris, N.B.W., Tindle, A.G., 1984. Trace element determination diagrams for the tectonic interpretation of granitic rocks. J. Petrol. 25, 956–983.
Polito, P.A., Kyser, K.T., Stanley, C., 2009. The Proterozoic, albitite-hosted, Valhalla uranium deposit, Queensland, Australia, a description of the alteration assemblage associated with uranium mineralisation in diamond drill hole V39. Miner. Deposita 44, 11–40.
Porter, T.M., 2010a. Current understanding of iron oxide associated-alkali altered mineralised systems: Part I—an overview. In: Porter, T.M. (Ed.), Hydrothermal Iron Oxide Copper-Gold and Related Deposits: A Global Perspective. Porter Geoscience Consultant Publications, Adelaide, pp. 5–32.
Porter, T.M., 2010b. Current understanding of iron oxide associated-alkali altered mineralised systems: Part II—a review. In: Porter, T.M. (Ed.), Hydrothermal Iron Oxide Copper-Gold and Related Deposits: A Global Perspective. Porter Geoscience Consultant Publications, Adelaide, pp. 33–106.
Porto de Silveira, C.L., Shorscher, H.D., Miekeley, N., 1991. The geochemistry of albitisation and related uranium mineralisation, Espinharas, Paraiba. Brazil. J. Geochem. Explor 40, 329–347.
Potter, E.G., Corriveau, L., Montreuil, J.-F., Yang, Z., Comeau, J.-S., 2014. Geochemical signatures of uraninite from iron oxide-copper-gold (IOCG) systems of the Great Bear magmatic zone, Canada. Geological Survey of Canada, Open File 7545, 1 sheet.
Potter, E.G., Montreuil, J.-F., Corriveau, L., Davis, W.J., 2019. The Southern Breccia Metasomatic Uranium System of the Great Bear Magmatic Zone, Canada: iron oxide-copper-gold (IOCG) and albitite-hosted uranium linkages. In: Decrée, S., Robb, L. (Eds.), Ore Deposits: Origin, Exploration, and Exploitation. American Geophysical Union, Geophysical Monograph, vol. 242, pp. 109–130.
Potter, E.G., Acosta-Gongora, P., Corriveau, L., Montreuil, J-F., Yang, Z., in press. Uranium enrichment in iron oxide and alkali-altered (IOAA) systems of the Great Bear magmatic zone as revealed by trace element signatures of uraninite. In: Corriveau, L., Potter, E.G., Mumin, A.H. (Eds.), Iron Oxide-Copper-Gold and Affiliated Deposits. Geological Association of Canada Special Paper 52.
Requia, K, et al., 2003. Re-Os and Pb-Pb geochronology of the Archean Salobo iron oxide copper-gold deposit, Carajás mineral province, northern Brazil. Mineralium Deposita 38 (6), 727–738.
Romberger, S.B., 1984. Transport and deposition of uranium in hydrothermal systems at temperatures up to 300 °C: geological implications. In: DeVivo, B., Ippolito, F., Capaldi, G., Simpson, P.R. (Eds.), Uranium Geochemistry, Mineralogy, Geology, Exploration and Resources. Institution of Mining and Metallurgy, London, pp. 12–17.
Rudnick, R.L., Gao, S., 2014. Composition of the continental crust. In: Rudnick, R.L., Holland, H.D., Turekian, K.K. (Eds.), Treatise on Geochemistry, second ed. Elsevier, Amsterdam, pp. 1–64.
Ryan, B. 1984. Regional geology of the central part of the Central Mineral Belt, Labrador. In: Government of Newfoundland and Labrador, Department of Mines and Energy, Mineral Development Division. Memoir, vol. 3, pp. 185.
Salvi, S., Fontan, F., Monchoux, P., Williams-Jones, A.E., Moine, B., 2000. Hydrothermal mobilization of high field strength elements in alkaline igneous systems: evidence from the Tamazeght Complex (Morocco). Econ. Geol. 95, 559–576.
Schärer, U., Krogh, T.E., Wardle, R.J., Ryan, B., Gandhi, S.S., 1988. U-Pb ages of early and middle Proterozoic volcanism and metamorphism in the Makkovik Orogen. Labrador. Can. J. Earth Sci. 25, 1098–1107. https://doi.org/10.1139/e88-107.
Skirrow, R., 2010. "Hematite-group" IOCG ± U ore systems: Tectonic settings, hydrothermal characteristics, and Cu-Au and U mineralizing processes. In: Corriveau, L., Mumin, A, (Eds.), Exploring for iron oxide copper-gold deposits: Canada and global analogues. Geological Association of Canada, Short Course Notes 20, pp. 39–58.
Sparkes, G., Kerr, A., 2008. Diverse styles of uranium mineralization in the Central Mineral Belt of Labrador: an overview and preliminary discussion. In: Current research, Newfoundland and Labrador Department of Natural Resources Geological Survey Report 08-1, pp. 193–227.
Sparkes, G.W., Dunning, G.R. McNicoll, V.J. 2010, New U–Pb age constraints and potential implications for the genesis of the Kitts uranium deposit, Central Mineral Belt, Labrador. In: Curr. Res., Rep. 10-1, pp. 93–109.
Sparkes, G., Dunning, G., Fonkwe, M., and Langille, A., 2016. Age constraints on the formation of the iron oxide-rich hydrothermal breccias of the Moran Lake area: evidence for potential IOCG-style mineralization within the Central Mineral Belt of Labrador. In: Newfoundland and Labrador Department of Natural Resources, Geological Survey Report 16–1, pp. 71–90.
Sparkes, G.W., Dunning, G.R., Langille, A, 2017. The Michelin deposit: an example of albitite-hosted uranium mineralization within the Central Mineral Belt of Labrador. In: Newfoundland and Labrador Department of Natural Resources Geological Survey, Report 17-1, pp. 219–238.
Sparkes, G., 2017. Uranium mineralization within the Central Mineral Belt of Labrador: a summary of the diverse styles, settings and timing of mineralization: Newfoundland and Labrador Department of Resources Open File LAB/1684.
Sidder, G.B., Day, W.C., Nuelle, L.M., Seeger, C.M., Kisvarsanyi, E.B., 1993. Mineralogic and fluid-inclusion studies of the Pea Ridge iron-rare-earth-element deposit, southeast Missouri. U.S. Geological Survey Bulletin 205–216 In this issue.
Sidor, M, 2000. The origin of the black rock alteration overprinting iron-rich sediments and its genetic relationship to disseminated polymetallic sulphide ores, Lou Lake, Northwest Territories, Canada, MSc Thesis. The University of Western Ontario In this issue.
Somarin, A.K., Mumin, A.H., 2014. P-T-composition and evolution of paleofluids in the

Paleoprotoerozoic Mag Hill IOCG system, Contact Lake belt, Northwest Territories, Canada. Mineralium Deposita 49 (2), 199–215.
Timofeev, A., Migdisov, A.A., Williams-Jones, A.E., Roback, R., Nelson, A.T., Xu, H., 2018. Uranium transport in acidic brines under reducing conditions. Nat. Commun. 9. https://doi.org/10.1038/s41467-018-03564-7.
Tracey, M., 2009. Study of Volcanic and Sediment-Hosted Uranium within the Post Hill Group, Central Mineral Belt Region, Labrador. Unpublished B.Sc. Thesis. Memorial University, Canada, pp. 137.
Wardle, R.J., Ryan, B., Nunn, G.A.G., Mengel, F.C., 1990. Labrador segment of the Trans-Hudson Orogen: crustal development through oblique convergence and collision. In: Early Proterozoic Trans-hudson Orogen of North America, Special Paper 37, pp. 353–369.
Wilde, A., 2013. Towards a model for albitite-type uranium. Minerals 3, 36–48.
Wilton, D.H.C., Longerich, H.P., 1993. Metallogenic significance of trace element and U-Pb isotope data for uraninite-rich mineral separates from the Labrador Central Mineral Belt. Can. J. Earth Sci. 30, 2352–2365. https://doi.org/10.1139/e93-204.
Wilton, D.H.C., Wardle, R.J., 1987. Two contrasting metallogenic styles in the Early Proterozoic Upper Aillik Group, Central Mineral Belt, Labrador, Canada. Miner. Deposita 22, 198–206. https://doi.org/10.1007/BF00206610.
Wood, S.A., 2005.The aqueous geochemistry of zirconium, hafnium, niobium and tantalum. In: Linnen, R.L., Samson, I.M. (Eds.), Rare-Element Geochemistry and Mineral Deposits, Geological Association of Canada Short Course Notes 17, pp. 217–250.